

A non-conforming least-squares finite element method for incompressible fluid flow problems

Pavel Bochev^{1,*}, James Lai² and Luke Olson²

¹*Numerical Analysis and Applications Department, Sandia National Laboratories, Mail Stop 1320, Albuquerque, NM 87185-1320, USA*

²*Department of Computer Science, University of Illinois at Urbana-Champaign, Urbana, IL 61801s, USA*

SUMMARY

In this paper, we develop least-squares finite element methods (LSFEMs) for incompressible fluid flows with improved mass conservation. Specifically, we formulate a new locally conservative LSFEM for the velocity–vorticity–pressure Stokes system, which uses a piecewise divergence-free basis for the velocity and standard C^0 elements for the vorticity and the pressure. The new method, which we term dV-VP improves upon our previous discontinuous stream-function formulation in several ways. The use of a velocity basis, instead of a stream function, simplifies the imposition and implementation of the velocity boundary condition, and eliminates second-order terms from the least-squares functional. Moreover, the size of the resulting discrete problem is reduced because the piecewise solenoidal velocity element is approximately one-half of the dimension of a stream-function element of equal accuracy. In two dimensions, the discontinuous stream-function LSFEM [1] motivates modification of our functional, which further improves the conservation of mass. We briefly discuss the extension of this modification to three dimensions. Computational studies demonstrate that the new formulation achieves optimal convergence rates and yields high conservation of mass. We also propose a simple diagonal preconditioner for the dV-VP formulation, which significantly reduces the condition number of the LSFEM problem. Published 2012. This article is a US Government work and is in the public domain in the USA.

Received 19 December 2011; Revised 12 September 2012; Accepted 10 October 2012

KEY WORDS: least-squares finite element methods; discontinuous elements; Stokes and Navier–Stokes equations; piecewise divergence-free velocity; stream function; vorticity; pressure; mass conservation

1. INTRODUCTION

Least-squares finite element methods (LSFEMs) for partial differential equations (PDEs) cast PDEs into unconstrained minimization problems for artificial least-squares ‘energy’ functionals. Summation of equation residuals measured in suitable Sobolev space norms defines the least-squares functional.

Least-squares methods offer valuable computational and theoretical properties. For example, norm-equivalent least-squares functionals give rise to symmetric, strongly coercive variational problems, and a stable and accurate finite element discretization does not require restrictive inf-sup conditions between the finite element spaces. As a result, the associated algebraic systems of equations are symmetric and positive definite, and are often amenable to efficient iterative methods such as preconditioned conjugate gradients.

However, one drawback in conventional C^0 LSFEMs for incompressible fluid flows is the lack of control of mass conservation, which in some cases leads to highly inaccurate results [2, 3].

*Correspondence to: Pavel Bochev, Sandia National Laboratories, Mail Stop 1320, Albuquerque, NM 87185-1320, USA.

†E-mail: pboche@sandia.gov

The published remedies include the restricted least-squares method [2], high-order (spectral and *hp*) least-squares methods [3, 4], and mimetic least-squares methods [5, Section 7.7], [6]. Although these approaches succeed in improving mass conservation, they remain more complex to implement than standard mixed Galerkin methods and often require non-standard boundary conditions and/or structured grids, thus conceding several of the advantages of least-squares principles. A study of mass and momentum conservation [3] reveals that least-squares methods possess excellent momentum conservation even when the mass is conserved poorly. These observations further motivate our focus on mass conservation as the most pressing task in least-squares formulations.

This paper continues the effort of Bochev *et al.* [1] to develop least-squares methods, which improve mass conservation, while remaining straightforward to implement and solve using publicly available libraries such as the Trilinos [7] packages Intrepid [8] and ML [9]. The discontinuous stream function, continuous vorticity, and pressure method (dS-VP) [1] uses a discontinuous stream function to obtain a locally divergence-free finite element solution of the Stokes equations. The method achieves nearly perfect conservation of mass on a series of challenging test problems, yet requires the use of an additional stream function.

In this paper, we present a new discontinuous velocity, continuous vorticity–pressure (dV-VP) LSFEM for the Stokes equations. Our goal is to develop alternatives that improve upon the dS-VP formulation by directly employing a piecewise solenoidal basis [10] for the velocity. As a result, we eliminate second-order terms from the least-squares functional, simplify implementation of the velocity boundary condition, and reduce the minimal admissible polynomial order from 3, in the dS-VP method, to 2, which is equal to that of the stable Taylor–Hood (TH) element pair [11]. Because the dimension of the piecewise solenoidal velocity element is approximately one-half of the dimension of a stream-function element with comparable accuracy, the size of the resulting algebraic problem is reduced. Introducing discontinuous terms also affects the conditioning of the problem. Yet, we demonstrate that a simple diagonal preconditioner is effective for the dV-VP algebraic problem.

In two dimensions, the dS-VP method motivates a simple modification of the dV-VP formulation, in which the least-squares functional is augmented with jumps of the integrals of the normal velocity component. Computational studies support this modification of the dV-VP LSFEM by showing optimal convergence rates and by highlighting the mass conservation properties in the approximation. We briefly explain how the modification extends to three dimensions.

In Section 2, we summarize the notation, the governing equations, and various least-squares formulations relevant to this paper and introduce test problems for the computational studies. In Section 3, we present the new dV-VP LSFEM by introducing a series of intermediate functionals. There, we also define a diagonal preconditioner for the discrete problems. In Section 4, we briefly discuss extension of the dV-VP formulation to the time-dependent Navier–Stokes equations, and in Section 5, we focus on computational studies, which include conservation of mass, convergence rates, preconditioning, and impact of the divergence-free basis choice on the properties of the LSFEMs. In particular, we compare the new dV-VP LSFEM with a suite of finite element methods including a least-squares formulation employing standard continuous nodal elements, an intermediate version of the dV-VP without the jumps of the integrals of the normal velocity component, and a mixed Galerkin formulation of the Stokes equations employing the classical TH element pair. The section also presents preliminary results for the Navier–Stokes equations obtained for the driven cavity flow problem. We summarize our conclusions in Section 6.

2. QUOTATION OF RESULTS

2.1. Notation

For clarity, we restrict our attention to two space dimensions and bounded, simply connected regions $\Omega \subset \mathbb{R}^2$ with a Lipschitz-continuous boundary $\Gamma = \partial\Omega$. We adhere to the standard notation, $H^k(\Omega)$, for a Sobolev space of order k with norm and inner product given by $\|\cdot\|_k$ and $(\cdot, \cdot)_k$, respectively. When $k = 0$, we write $L^2(\Omega)$, (\cdot, \cdot) , and $\|\cdot\|_0$. The subspace of $H^1(\Omega)$ functions with vanishing trace on $\partial\Omega$ is $H_0^1(\Omega)$ and $L_0^2(\Omega)$ is the subspace of L^2 -fields with zero mean. We denote

by $H^{-1}(\Omega)$ the dual of $H_0^1(\Omega)$ with norm

$$\|u\|_{-1} = \sup_{v \in H_0^1(\Omega)} \frac{(u, v)}{\|v\|_1}. \tag{1}$$

Vectors and vector valued function spaces are denoted by boldface symbols—for example, $\mathbf{u} = (u_1, u_2)$ and $\mathbf{H}^1(\Omega)$ —with the Euclidean norm on \mathbb{R}^2 given by $|\cdot|$. In two dimensions, the curl is defined for scalar and vector functions by

$$\nabla \times \omega = \begin{bmatrix} \omega_y \\ -\omega_x \end{bmatrix} \quad \text{and} \quad \nabla \times \mathbf{u} = (u_2)_x - (u_1)_y, \tag{2}$$

respectively.

We consider a conforming finite element partition $\mathcal{K}_h = \{\kappa\}$ of the domain Ω , where, in two dimensions, κ is either a quadrilateral or a triangle. Two neighboring elements share an edge, ε , and we denote the set of all edges in the mesh \mathcal{K}_h as \mathcal{E}_h , the set of all interior edges as $\mathcal{E}_{h,0}$, and the set of all boundary edges as $\mathcal{E}_{h,\Gamma}$.

The discontinuous methods in this paper use standard jump operators on element interfaces. Let κ^+ and κ^- be two adjacent elements that share edge ε , and let ψ^+ and ψ^- be the restrictions of a piecewise smooth function ψ on these elements. The jump of ψ across the interface is the difference of its states along ε :

$$[\psi] := (\psi^+ - \psi^-)|_\varepsilon. \tag{3}$$

Furthermore, a component-wise application of the scalar jump operator (3) defines a jump operator for a piecewise smooth vector field \mathbf{u} :

$$[\mathbf{u}] := ([u_1], [u_2]). \tag{4}$$

2.2. Standard C^0 finite element spaces

We assume that \mathcal{K}_h is quasi-uniform [12], where the elements in \mathcal{K}_h are images of a standard (reference) element $\widehat{\kappa}$ under a smooth map $F_\kappa : \widehat{\kappa} \mapsto \kappa$, where $J_\kappa = \nabla F_\kappa$. The approximating space on each element is defined by suitable transformation of the reference space $R_r(\widehat{\kappa})$. In the case of a simplex $\widehat{\kappa}$, $R_r(\widehat{\kappa}) = P_r(\widehat{\kappa})$ is the space of all polynomials of degree r , whereas in the case of a square $\widehat{\kappa}$, $R_r(\widehat{\kappa}) = Q_r(\widehat{\kappa})$ is the space of all polynomials whose degree in each coordinate direction does not exceed r .

The standard C^0 finite element spaces of degree $r > 0$ on quadrilateral and triangular grids are

$$R_r(\Omega) = \{v_h \in H^1(\Omega) \mid v_h|_\kappa = \widehat{v}_h \circ F_\kappa^{-1}; \widehat{v}_h \in R_r(\widehat{\kappa})\}. \tag{5}$$

Here, $[R_r](\Omega)$ is the discontinuous version of these spaces. The coefficients of a finite element function v_h relative to a basis are a vector $\vec{v} \in \mathbb{R}^n$.

Next, we recall several key properties of standard finite elements (5) on quasi-uniform grids.

Approximation. For every $v \in H^{r+1}(\Omega)$, there exists $I(v) \in R_r(\Omega)$ such that

$$\|v - I(v)\|_0 + h\|v - I(v)\|_1 \leq Ch^{r+1}\|v\|_{r+1}, \tag{6}$$

where C is independent of h .

Inverse inequalities. There exist positive constants C_1 and C_2 , independent of h , such that for every element $\kappa \in \mathcal{K}_h$

$$C_1h^2|\vec{v}|^2 \leq \|v_h\|_{0,\kappa}^2 \leq C_2h^2|\vec{v}|^2. \tag{7}$$

Additionally, finite element functions satisfy the inverse inequalities

$$\|v_h\|_{1,\kappa} \leq Ch^{-1}\|v_h\|_{0,\kappa} \quad \text{and} \quad \|v_h\|_{1/2,e} \leq Ch^{-1/2}\|v_h\|_{0,e}. \tag{8}$$

These inequalities hold whenever the mesh is quasi-uniform, and the finite element spaces are defined by transformation of a reference space as in (5) [13, Lemma 9.7, p. 386; Lemma 1.138, p. 75]. In finite element methods that involve mesh-dependent terms, such as weighted least-squares methods and discontinuous finite element methods, validity of inverse inequalities is required to maintain the proper scaling of these mesh-dependent terms.

2.3. Piecewise divergence-free velocity element

In this paper, we use a piecewise solenoidal velocity element V_r , with $r \geq 1$, as proposed in [10]. The dimension of V_r depends only on the polynomial degree r and not on the shape of the reference element $\hat{\kappa}$. For example, the linear piecewise solenoidal space in two dimensions is

$$V_1(\hat{\kappa}) = \left\{ \begin{pmatrix} 1 \\ 0 \end{pmatrix}, \begin{pmatrix} 0 \\ 1 \end{pmatrix}, \begin{pmatrix} y \\ 0 \end{pmatrix}, \begin{pmatrix} 0 \\ x \end{pmatrix}, \begin{pmatrix} x \\ -y \end{pmatrix} \right\}, \quad (9)$$

whereas the quadratic space is

$$V_2(\hat{\kappa}) = V_1(\hat{\kappa}) \cup \left\{ \begin{pmatrix} y^2 \\ 0 \end{pmatrix}, \begin{pmatrix} 0 \\ x^2 \end{pmatrix}, \begin{pmatrix} x^2 \\ -2xy \end{pmatrix}, \begin{pmatrix} -2xy \\ y^2 \end{pmatrix} \right\}. \quad (10)$$

In d dimensions, we arrive at

$$\dim V_r(\hat{\kappa}) = \frac{d(d+r)! - (d+r-1)!r}{d!r!}.$$

We define the full velocity space $V_r(\Omega)$ by translation and scaling of the reference element space

$$V_r(\Omega) = \left\{ \mathbf{v}_h \in L^2(\Omega) \mid \mathbf{v}_h(\mathbf{x})|_{\kappa} = \hat{\mathbf{v}}_h(\mathbf{x} - \mathbf{b}_{\kappa}) / J_{\kappa}^{(\deg \hat{\mathbf{v}})/2}; \hat{\mathbf{v}}_h \in V_r(\hat{\kappa}) \right\}, \quad (11)$$

where $\deg \hat{\mathbf{v}}$ is the polynomial degree of basis function $\hat{\mathbf{v}}_h$, and \mathbf{b}_{κ} is the center of mass of κ .

Remark 1

Inequalities such as (7) and (8) motivate the mesh-dependent weights in weighted least-squares functionals. However, the varying polynomial degrees of the basis functions in $V_r(\hat{\kappa})$ prevent (7) and (8) from holding. By using translation and mesh-dependent scaling proportional to the polynomial degree of each basis function, we are able to define piecewise solenoidal bases for $V_r(\Omega)$ that satisfy inverse inequalities. We note that this is similar to the piecewise divergence-free basis defined in [14]. However, the latter uses a different scaling for which the mass matrix is not spectrally equivalent to a scaled identity.

The velocity space (11) is completely discontinuous and is not H^1 -conforming, yet $V_r(\Omega)$ exhibits an optimal approximation property [10, Theorem 4.3]: For every $\mathbf{v} \in \mathbf{H}^{r+1}(\kappa)$, there exists $I(\mathbf{v}) \in V_r(\kappa)$ such that

$$\|\mathbf{v} - I(\mathbf{v})\|_{j,\kappa} \leq Ch^{r+1-j} |\mathbf{v}|_{r+1,\kappa}; \quad j = 0, \dots, r. \quad (12)$$

For examples of discontinuous Galerkin methods, which use V_r elements, we refer to [14, 15] and the references therein. The paper [10] also compares V_r elements with other non-conforming spaces such as the Crouzeix–Raviart elements [16].

2.4. The velocity–vorticity–pressure Stokes system

It is common to define LSFEMs by using the first-order system form of the governing PDEs. The Stokes equations admit several such forms [5, Section 7.1]. Here, we choose to work with the velocity–vorticity–pressure (VVP) first-order system

$$\nabla \times \omega + \nabla p = \mathbf{f} \quad \text{on } \Omega \quad (13a)$$

$$\omega - \nabla \times \mathbf{u} = 0 \quad \text{on } \Omega \quad (13b)$$

$$\nabla \cdot \mathbf{u} = 0 \quad \text{on } \Omega. \quad (13c)$$

The system (13) is augmented with the velocity boundary condition

$$\mathbf{u} = 0 \quad \text{on } \partial\Omega \quad (14)$$

and the zero mean pressure constraint

$$\int_{\Omega} p \, d\Omega = 0. \quad (15)$$

Each component of (13) plays a role in the solution: (13a) governs conservation of momentum, (13b) defines the vorticity, and (13c) is the continuity equation, which governs conservation of mass. The VVP Stokes equations have been studied extensively in the context of LSFEMs [17–23], and the mathematical and computational properties of conforming LSFEMs for (13) are well understood.

2.5. Standard C^0 least-squares methods for the velocity–vorticity–pressure Stokes system

We next review two conforming LSFEMs for (13), which motivate the new methods proposed in this paper. In both cases, the starting point is the least-squares functional

$$J_{-1}(\mathbf{u}, \omega, p; \mathbf{f}) = \|\nabla \times \omega + \nabla p - \mathbf{f}\|_{-1}^2 + \|\nabla \times \mathbf{u} - \omega\|_0^2 + \|\nabla \cdot \mathbf{u}\|_0^2, \quad (16)$$

which is norm equivalent on $X = \mathbf{H}_0^1(\Omega) \times L^2(\Omega) \times L_0^2(\Omega)$ —see [24]. Norm equivalence leads to a well-posed formulation of the least-squares, unconstrained minimization problem: Find $(\mathbf{u}, \omega, p) \in X$ such that

$$J_{-1}(\mathbf{u}, \omega, p; \mathbf{f}) \leq J_{-1}(\mathbf{v}, \xi, q; \mathbf{f}) \quad \forall (\mathbf{v}, \xi, q) \in X. \quad (17)$$

Here, the unique minimizer coincides with the solution of the VVP Stokes system (13).

A specific LSFEM emerges by choosing an approximation to the $\|\cdot\|_{-1}$ term in (16). One method is the *weighted* LSFEM [17]

$$J_h(\mathbf{u}_h, \omega_h, p_h; \mathbf{f}) = h^2 \|\nabla \times \omega_h + \nabla p_h - \mathbf{f}\|_0^2 + \|\nabla \times \mathbf{u}_h - \omega_h\|_0^2 + \|\nabla \cdot \mathbf{u}_h\|_0^2 \quad (18)$$

in which the negative norm is approximated by the weighted L^2 norm $h\|\cdot\|_0$, whereas another method is the *discrete negative norm* LSFEM

$$J_{-h}(\mathbf{u}_h, \omega_h, p_h; \mathbf{f}) = \|\nabla \times \omega_h + \nabla p_h - \mathbf{f}\|_{-h}^2 + \|\nabla \times \mathbf{u}_h - \omega_h\|_0^2 + \|\nabla \cdot \mathbf{u}_h\|_0^2 \quad (19)$$

in which the negative norm is approximated by $\|\cdot\|_{-h}^2 = h^2 \|\cdot\|_0^2 + \|(\mathcal{L}_h)^{1/2} \cdot\|_0^2$, where \mathcal{L}_h is a spectrally equivalent preconditioner for the Laplace operator [25]. For brevity, we denote both norms and the associated least-squares functionals by the common symbols $\|\cdot\|_{(h)}$ and $J_{(h)}$, respectively.

A well-posed discrete least-squares principle for (18) and (19) is the following: Find $(\mathbf{u}_h, \omega_h, p_h) \in X_h^r$ such that

$$J_{(h)}(\mathbf{u}_h, \omega_h, p_h; \mathbf{f}) \leq J_{(h)}(\mathbf{v}_h, \xi_h, q_h; \mathbf{f}) \quad \forall (\mathbf{v}_h, \xi_h, q_h) \in X_h^r, \quad (20)$$

where

$$X_h^r = \mathbf{R}_r(\Omega) \cap \mathbf{H}_0^1(\Omega) \times R_{r-1}(\Omega) \times R_{r-1}(\Omega) \cap L_0^2(\Omega) \quad (21)$$

with $r \geq 1$ for the discrete negative norm LSFEM, and $r > 1$ for the weighted[‡] LSFEM.

Both least-squares methods converge optimally for all sufficiently regular solutions of (13), as summarized in the following, whereas additional theoretical and computational properties of (19) and (18) are found in [5].

Theorem 1 (Optimal convergence [5, Theorem 7.14, p. 262])

Let $(\mathbf{u}_h, \omega_h, p_h) \in X_h^r$ with $r > 1$ be a solution to (18) and assume that $(\mathbf{u}, \omega, p) \in \mathbf{H}^{r+2}(\Omega) \times$

[‡]The *minimal approximation condition* $r > 1$ is required for optimal convergence rates in (18). Using $R_1(\Omega)$ elements for all variables in (21), for example, reduces the accuracy of the least-squares solution in (18); see [17].

$H^{r+1}(\Omega) \times H^{r+1}(\Omega)$ is the exact solution of the VVP Stokes system (13). There exists a constant $C > 0$ such that

$$\|\mathbf{u} - \mathbf{u}_h\|_1 + \|\omega - \omega_h\|_0 + \|p - p_h\|_0 \leq Ch^{r+1} (\|\mathbf{u}\|_{r+2} + \|\omega\|_{r+1} + \|p\|_{r+1}) \tag{22a}$$

and

$$\|\omega - \omega_h\|_1 + \|p - p_h\|_1 \leq Ch^r (\|\mathbf{u}\|_{r+2} + \|\omega\|_{r+1} + \|p\|_{r+1}). \tag{22b}$$

The error estimate (22) holds for (19) provided $r \geq 1$.

Remark 2

The error estimates in Theorem 1 hold for the equal-order spaces

$$X_h^{(r)} = \mathbf{R}_r(\Omega) \cap \mathbf{H}_0^1(\Omega) \times R_r(\Omega) \times R_r(\Omega) \cap L_0^2(\Omega). \tag{23}$$

where as before $r > 1$ when using the weighted functional (18). Such spaces have more degrees of freedom, but their uniform data structure simplifies implementation of least-squares methods.

2.6. *Discontinuous stream function, vorticity–pressure least-squares method (dS-VP)*

The approach presented in [1] is to consider discontinuous velocity fields in (18) and (19) and then to represent the velocity on each element by a curl of a discontinuous stream function. The resulting *discontinuous stream function, continuous vorticity–pressure* (dS-VP) version of $J_{(h)}$ is given by

$$\begin{aligned} J_{(h)}^S(\psi_h, \omega_h, p_h; \mathbf{f}) = & \|\nabla \times \omega_h + \nabla p_h - \mathbf{f}\|_{(h)}^2 + \sum_{\kappa \in \mathcal{K}_h(\Omega)} \|\nabla \times \nabla \times \psi_h - \omega_h\|_{0,\kappa}^2 \\ & + \sum_{\epsilon \in \mathcal{E}_{h,0}} h^{-1} \|[\nabla \times \psi_h]\|_{0,\epsilon}^2 + h^{-3} \|[\psi_h]\|_{0,\epsilon}^2 + \sum_{\epsilon \in \mathcal{E}_{h,\Gamma}} h^{-1} \|(\nabla \times \psi_h) \times \mathbf{n}_i\|_{0,\epsilon}^2. \end{aligned} \tag{24}$$

Computational results in [1] confirm that the dS-VP formulation attains high mass conservation. Substitution of the stream function by a vector potential \mathbf{a}_h such that $\mathbf{u}_h = \nabla \times \mathbf{a}_h$ extends (24) to three dimensions. Our key objective is to achieve similar mass conservation while avoiding some practical inconveniences of stream functions and vector potentials. As an example, for the velocity boundary condition, a Dirichlet boundary condition for the stream function requires solving the equation $(\nabla \times \psi) \cdot \mathbf{n} = \mathbf{u} \cdot \mathbf{n}$ for ψ on the boundary, while still requiring enforcement of the tangential velocity component. For the weighted LSFEM (18), the minimal approximation condition $r > 1$ implies that the stream function requires approximation by at least cubic or bi-cubic elements. These elements have nearly twice the degrees of freedom of the piecewise solenoidal element (9) and require more accurate quadrature than quadratic elements. Additionally, the second-order terms in (24) also result in higher condition numbers, leading to increased computational demands on the algebraic solver.

3. DISCONTINUOUS VELOCITY VORTICITY–PRESSURE LEAST-SQUARES METHOD

For clarity, we develop the new dV-VP formulation in three stages. The first stage reprises the approach of [1] to relax the C^0 continuity for the velocity space only. Therefore, we change the approximating space from (21) to

$$\widetilde{X}_h^r = [\mathbf{R}_r](\Omega) \cap \mathbf{H}_0^1(\Omega) \times R_{r-1}(\Omega) \times R_{r-1}(\Omega) \cap L_0^2(\Omega) \tag{25}$$

or its equal-order counterpart

$$\widetilde{X}_h^{(r)} = [\mathbf{R}_r](\Omega) \cap \mathbf{H}_0^1(\Omega) \times R_r(\Omega) \times R_r(\Omega) \cap L_0^2(\Omega) \tag{26}$$

and modify $J_{(h)}$ in (18) and (19) to allow discontinuous velocity fields:

$$\begin{aligned}
 J_{(h)}^V(\mathbf{u}_h, \omega_h, p_h; \mathbf{f}) = & \|\nabla \times \omega_h + \nabla p_h - \mathbf{f}\|_{(h)}^2 + \sum_{\kappa \in \mathcal{K}_h(\Omega)} \left(\|\nabla \times \mathbf{u}_h - \omega_h\|_{0,\kappa}^2 + \|\nabla \cdot \mathbf{u}_h\|_{0,\kappa}^2 \right) \\
 & + \sum_{\varepsilon \in \mathcal{E}_{h,0}} h^{-1} \|\llbracket \mathbf{u}_h \rrbracket\|_{0,\varepsilon}^2.
 \end{aligned}
 \tag{27}$$

Numerical results in [1] show that (27) conserves mass poorly even if tangential and normal jumps of the velocity are weighted differently. To improve mass conservation in [1], we used a discontinuous stream function and the associated dS-VP formulation (24). In this paper, we adopt a different approach and approximate the velocity directly using the piecewise solenoidal discontinuous space $V_r(\Omega)$ as defined in Section 2.3. Thus, at the second stage, we replace the discrete minimization spaces (25) and (26) by

$$\overline{X}_h^r = V_r(\Omega) \times R_{r-1}(\Omega) \times R_{r-1}(\Omega) \cap L_0^2(\Omega)
 \tag{28}$$

and its equal-order analogue

$$\overline{X}_h^{(r)} = V_r(\Omega) \times R_r(\Omega) \times R_r(\Omega) \cap L_0^2(\Omega),
 \tag{29}$$

respectively, where $r > 1$ if $\|\cdot\|_{(h)}$ is the weighted L^2 norm, and $r \geq 1$ if $\|\cdot\|_{(h)}$ is the discrete negative norm. The degrees of freedom in $V_r(\Omega)$ are not point values of the velocity field. As a result, strong imposition of the velocity boundary condition requires solving a simple linear system on each element that has an edge in $\mathcal{E}_{h,\Gamma}$. Alternatively, we can impose (14) weakly by including an appropriate residual in the least-squares functional. In this paper, we adopt the latter approach because of its simplicity. Taking this and the divergence-free property of the velocity basis into consideration, we introduce a new functional

$$\begin{aligned}
 \widehat{J}_{(h)}^{V,\alpha}(\mathbf{u}_h, \omega_h, p_h; \mathbf{f}) = & \|\nabla \times \omega_h + \nabla p_h - \mathbf{f}\|_{(h)}^2 + \sum_{\kappa \in \mathcal{K}_h(\Omega)} \|\nabla \times \mathbf{u}_h - \omega_h\|_{0,\kappa}^2 \\
 & + \sum_{\varepsilon \in \mathcal{E}_{h,0}} h^{-\alpha} \|\llbracket \mathbf{u}_h \rrbracket\|_{0,\varepsilon}^2 + \sum_{\varepsilon \in \mathcal{E}_{h,\Gamma}} h^{-\alpha} \|\mathbf{u}_h\|_{0,\varepsilon}^2.
 \end{aligned}
 \tag{30}$$

We determine the weight α as follows. A straightforward dimensional analysis shows that for the solenoidal vector fields in (11) and standard nodal functions $\psi_h \in [R_r](\Omega)$, we have

$$\int_{\varepsilon} \llbracket \mathbf{u}_h \rrbracket^2 dl = O(h) \quad \text{and} \quad \int_{\varepsilon} [\nabla \times \psi_h]^2 dl = O(h^{-1}),
 \tag{31}$$

for some edge $\varepsilon \in \mathcal{E}_h$. Therefore, in order to preserve the relative scaling of the terms in the dS-VP functional (24) when using the piecewise solenoidal space (11), it is necessary to change the weight of the velocity jump term from h^{-1} to h^{-3} . Taking this into consideration, for the divergence-free velocity spaces (28) and (29), we replace (27) by

$$\widehat{J}_{(h)}^V(\mathbf{u}_h, \omega_h, p_h; \mathbf{f}) := \widehat{J}_{(h)}^{V,-3}(\mathbf{u}_h, \omega_h, p_h; \mathbf{f}).
 \tag{32}$$

This formulation is applicable to both two-dimensional and three-dimensional configurations.

Remark 3

Divergence-conforming elements such as the Raviart–Thomas element [26] present a potential alternative to the piecewise solenoidal basis (11). In these elements, the normal component of the velocity is continuous across element interfaces. As a result, (30) only needs to include the jump of the tangential velocity component on element interfaces. Likewise, the normal part of the velocity boundary condition could be imposed strongly, whereas the no-slip condition would have to be imposed weakly by including an appropriate residual in the least-squares functional.

However, straightforward approximation of the velocity by div-conforming elements faces some difficulties in the context of the VVP Stokes formulations. Specifically, div-conforming elements are not in the domain of the curl operator, which makes it impossible to implement the residual of $\nabla \times \mathbf{u}_h - \omega_h$ directly. Instead, the curl operator is replaced with a discrete version $\nabla^h \times$ (cf. [6]). The discrete curl operator requires inversion of a mass matrix, leads to non-sparse matrices, and adds additional complexity to the implementation of the method. For this reason, we do not pursue div-conforming elements in this paper. We refer to [27, 28] for examples of methods that use this element in the context of the velocity–pressure formulation where this problem does not arise.

3.1. Implicit stream-function modification in 2D

In this section, we motivate the modification of (32) by additional jump terms, to further enhance its mass conservation in two dimensions. In this case, there is a global scalar stream function ψ such that the exact velocity $\mathbf{u} = \nabla \times \psi$. The divergence-free least-squares velocity approximation $\mathbf{u}_h \in \mathbf{V}_r(\Omega)$ has this property locally—that is, on every element $\kappa \in \mathcal{K}_h$, there is an implicit stream function ψ_κ such that $\mathbf{u}_h|_\kappa = \nabla \times \psi_\kappa$. Yet, the existence of an implicit stream function ψ_κ on each element does not imply that the piecewise solenoidal field $\mathbf{u}_h \in \mathbf{V}_r(\Omega)$ approximates the curl of the *global* stream function ψ . This requires the implicit stream functions ψ_κ on adjacent elements to be nearly equal along the interfaces between the elements. In contrast, the jump in velocity in (32) only controls the continuity of $\nabla \times \psi_\kappa$ and does not directly ‘glue’ ψ_κ across element interfaces. To enforce this on the implicit stream functions, we propose to augment (32) with terms that imitate the jumps of the discontinuous stream function in (24).

For simplicity, we express the main idea by using the trapezoidal rule to approximate the line integrals in these jumps. Let $V_0 = V_0(\varepsilon)$ and $V_1 = V_1(\varepsilon)$ be the endpoints of edge $\varepsilon \in \mathcal{E}_h$. Then

$$\int_\varepsilon [\psi_h]^2 d\ell \approx \frac{|\varepsilon|}{2} ([\psi_h(V_0)]^2 + [\psi_h(V_1)]^2). \tag{33}$$

Implementation of this formula requires reconstruction of the implicit stream-function values at V_0 and V_1 using the piecewise solenoidal velocity field. To this end, we denote the two elements that share an edge $\varepsilon = (\varepsilon_1, \varepsilon_2)$ by $\kappa^+(\varepsilon)$ and $\kappa^-(\varepsilon)$. The unit normal and the unit tangent to ε are \mathbf{n} and \mathbf{t} , respectively. For a given $\mathbf{u}_h \in \mathbf{V}_r(\Omega)$, let ψ_k^+ and ψ_k^- denote its implicit stream functions on each $\kappa^+(\varepsilon)$ and $\kappa^-(\varepsilon)$, respectively:

$$\mathbf{u}_h^\pm = (u_{h,1}^\pm, u_{h,2}^\pm) = \mathbf{u}_h|_{\kappa^\pm(\varepsilon)} = (\partial_y \psi_k^\pm, -\partial_x \psi_k^\pm). \tag{34}$$

Solving for the gradients of the implicit stream functions yields

$$\nabla \psi_k^\pm = (-u_{h,2}^\pm, u_{h,1}^\pm). \tag{35}$$

As a result, along edge ε

$$\frac{d\psi_k^\pm}{ds} \Big|_\varepsilon = \nabla \psi_k^\pm \cdot \mathbf{t} = (u_{h,1}^\pm \varepsilon_2 - u_{h,2}^\pm \varepsilon_1) = \mathbf{u}_h^\pm \times \mathbf{t} = \mathbf{u}^\pm \cdot \mathbf{n}. \tag{36}$$

The values of the implicit stream functions ψ_k^\pm at V_0 and V_1 can be determined by solving the edge ODEs

$$\begin{cases} \frac{d\psi_k^\pm}{ds} \Big|_\varepsilon = (\mathbf{u}^\pm \cdot \mathbf{n}) \Big|_\varepsilon \\ \psi_k^\pm(0) = C_0 \end{cases} \quad \text{and} \quad \begin{cases} \frac{d\psi_k^\pm}{ds} \Big|_\varepsilon = -(\mathbf{u}^\pm \cdot \mathbf{n}) \Big|_\varepsilon \\ \psi_k^\pm(|\varepsilon|) = C_1 \end{cases} \tag{37}$$

for $0 < s < |\varepsilon|$. Solving (37) yields

$$\psi_k^\pm(V_1) = C_0 + \int_\varepsilon \mathbf{u}^\pm \cdot \mathbf{n} d\ell \quad \text{and} \quad \psi_k^\pm(V_0) = C_1 - \int_\varepsilon \mathbf{u}^\pm \cdot \mathbf{n} d\ell. \tag{38}$$

Then using (38) in (33) gives the approximation

$$\int_{\varepsilon} [\psi_h]^2 d\ell \approx \frac{|\varepsilon|}{2} \left(\left[\int_{\varepsilon} \mathbf{u} \cdot \mathbf{n} d\ell \right]^2 + \left[\int_{\varepsilon} \mathbf{u} \cdot (-\mathbf{n}) d\ell \right]^2 \right) = |\varepsilon| \left[\int_{\varepsilon} \mathbf{u} \cdot \mathbf{n} d\ell \right]^2. \tag{39}$$

Thus, the implicit stream-function modification of (32) adds properly weighted terms (39) to the least-squares functional:

$$\begin{aligned} \widehat{J}_{(h)}^{V,-3,\beta}(\mathbf{u}_h, \omega_h, p_h; \mathbf{f}) &= \|\nabla \times \omega_h + \nabla p_h - \mathbf{f}\|_{(h)}^2 + \sum_{\kappa \in \mathcal{K}_h(\Omega)} \|\nabla \times \mathbf{u}_h - \omega_h\|_{0,\kappa}^2 \\ &+ \sum_{\varepsilon \in \mathcal{E}_{h,0}} \left(h^{-3} \|\llbracket \mathbf{u}_h \rrbracket\|_{0,\varepsilon}^2 + h^{-\beta} |\varepsilon| \left[\int_{\varepsilon} \mathbf{u}_h \cdot \mathbf{n} d\ell \right]^2 \right) + \sum_{\varepsilon \in \mathcal{E}_{h,\Gamma}} h^{-3} \|\mathbf{u}_h\|_{0,\varepsilon}^2. \end{aligned} \tag{40}$$

For grids aligned with the coordinate axes, the integral jump in (40) is straightforward to compute exactly. On general unstructured grids, we approximate the integral jumps by using three-point Gauss quadrature along each edge. To determine the weight β in (40), observe that dimensional analysis of the terms yields

$$|\varepsilon| \left[\int_{\varepsilon} \mathbf{u}_h \cdot \mathbf{n} d\ell \right]^2 = O(h^3) \quad \text{and} \quad \int_e [\psi_h]^2 dl = O(h). \tag{41}$$

In the dS-VP functional (24), we weight the integral of $[\psi_h]^2$ along ε by h^{-3} . Therefore, to reproduce the relative scaling of the terms in the dS-VP, we set $\beta = -5$. With this choice, we arrive at the final form of the modified least-squares functional:

$$\begin{aligned} \widetilde{J}_{(h)}^V(\mathbf{u}_h, \omega_h, p_h; \mathbf{f}) &= \|\nabla \times \omega_h + \nabla p_h - \mathbf{f}\|_{(h)}^2 + \sum_{\kappa \in \mathcal{K}_h(\Omega)} \|\nabla \times \mathbf{u}_h - \omega_h\|_{0,\kappa}^2 \\ &+ \sum_{\varepsilon \in \mathcal{E}_{h,0}} \left(h^{-3} \|\llbracket \mathbf{u}_h \rrbracket\|_{0,\varepsilon}^2 + h^{-5} |\varepsilon| \left[\int_{\varepsilon} \mathbf{u}_h \cdot \mathbf{n} d\ell \right]^2 \right) + \sum_{\varepsilon \in \mathcal{E}_{h,\Gamma}} h^{-3} \|\mathbf{u}_h\|_{0,\varepsilon}^2. \end{aligned} \tag{42}$$

Remark 4

Whereas the piecewise solenoidal fields $\mathbf{u}_h \in \mathbf{V}_r(\Omega)$ are curls of discontinuous implicit stream functions $\psi \in [R]_{r+1}(\Omega)$, the modified dV-VP least-squares method (42) is not equivalent to the dS-VP formulation (24) and has some important computational advantages. First, it does not contain second-order derivatives, which helps to reduce the conditioning of the resulting algebraic systems. Second, because the stream function is approximated by polynomials of one degree higher than the velocity, (24) requires more accurate (and more expensive) quadrature than (42). Third, for moderate polynomial degrees, the dimension of $[R]_{r+1}(\Omega)$ is almost twice that of the piecewise solenoidal space $\mathbf{V}_r(\Omega)$.

Remark 5

Extension of the implicit stream-function modification to three dimensions requires recovery of an implicit vector potential \mathbf{a}_κ such that $\mathbf{u}_h|_\kappa = \nabla \times \mathbf{a}_\kappa$ on every element. While possible, this task is more computationally intensive, as it requires solution of a div-curl system

$$\nabla \times \mathbf{a}_\kappa = \mathbf{u}_h \quad \text{and} \quad \nabla \cdot \mathbf{a}_\kappa = 0 \quad \text{in } \kappa$$

for the vector potential on every element. Assume that \mathbf{a}_h is the recovered (discontinuous) vector potential. The three-dimensional version of (42) then assumes the form

$$\begin{aligned} \widetilde{J}_{(h)}^V(\mathbf{u}_h, \omega_h, p_h; \mathbf{f}) &= \|\nabla \times \omega_h + \nabla p_h - \mathbf{f}\|_{(h)}^2 + \sum_{\kappa \in \mathcal{K}_h(\Omega)} \|\nabla \times \mathbf{u}_h - \omega_h\|_{0,\kappa}^2 \\ &+ \sum_{s \in \mathcal{S}_{h,0}} \left(h^{-3} \|\llbracket \mathbf{u}_h \rrbracket\|_{0,s}^2 + h^{-3} \|\llbracket \mathbf{a}_h \rrbracket\|_{0,s}^2 \right) + \sum_{s \in \mathcal{S}_{h,\Gamma}} h^{-3} \|\mathbf{u}_h\|_{0,s}^2, \end{aligned}$$

where $\mathcal{S}_{h,0}$ are interior element sides, and $\mathcal{S}_{h,\Gamma}$ are the sides on the boundary Γ .

3.2. Preconditioning of the algebraic equations

We denote \mathbb{K} as the symmetric and positive definite matrix resulting from the dV-VP least-squares functional (42). For a test function $(\mathbf{u}_i, \omega_i, p_i) \in \bar{X}_h^r$, or $(\mathbf{u}_i, \omega_i, p_i) \in \bar{X}_h^{(r)}$, we see that the weak form of (42) leads to the following 3×3 system for \mathbb{K} :

$$\begin{pmatrix} \mathbb{K}_{\mathbf{u},\mathbf{u}} & \mathbb{K}_{\mathbf{u},\omega} & \mathbf{0} \\ \mathbb{K}_{\mathbf{u},\omega} & \mathbb{K}_{\omega,\omega} & \mathbb{K}_{\omega,p} \\ \mathbf{0} & \mathbb{K}_{\omega,p} & \mathbb{K}_{p,p} \end{pmatrix} \begin{pmatrix} \vec{\mathbf{u}} \\ \vec{\omega} \\ \vec{p} \end{pmatrix} = \begin{pmatrix} f_{\mathbf{u}} \\ f_{\omega} \\ f_p \end{pmatrix} \tag{43}$$

where

$$\begin{aligned} (\mathbb{K}_{\mathbf{u},\mathbf{u}})_{ij} &= \sum_k (\nabla \times \mathbf{u}_i, \nabla \times \mathbf{u}_j)_{0,k} + \sum_{\varepsilon \in \mathcal{E}_{h,\Gamma}} h^{-3}([\mathbf{u}_i], [\mathbf{u}_j])_{0,\varepsilon} \\ &+ \sum_{\varepsilon \in \mathcal{E}_{h,0}} \left(h^{-3}([\mathbf{u}_i], [\mathbf{u}_j])_{0,\varepsilon} + h^{-5}|\varepsilon| \left[\int_{\varepsilon} \mathbf{u}_i \cdot \mathbf{n} \, d\ell \right] \left[\int_{\varepsilon} \mathbf{u}_j \cdot \mathbf{n} \, d\ell \right] \right) \end{aligned} \tag{44}$$

and

$$(\mathbb{K}_{\mathbf{u},\omega})_{ij} = (\nabla \times \mathbf{u}_i, \omega_j), \tag{45a}$$

$$(\mathbb{K}_{\omega,\omega})_{ij} = h^2 (\nabla \times \omega_i, \nabla \times \omega_j), \tag{45b}$$

$$(\mathbb{K}_{\omega,p})_{ij} = h^2 (\nabla \times \omega_i, \nabla p_j) = h^2 (\mathbf{n} \times \omega, \nabla p)_{0,\Gamma}, \tag{45c}$$

$$(\mathbb{K}_{p,p})_{ij} = h^2 (\nabla p_i, \nabla p_j). \tag{45d}$$

The h^2 weights arise from the use of the mesh-dependent norm $\|\cdot\|_{(h)} = h\|\cdot\|_0$. Dimensional analysis of the blocks in \mathbb{K} suggests the approximation

$$\mathbb{K} \sim \tilde{\mathbb{K}} = \begin{pmatrix} h^{-2}\mathbb{M}_{\mathbf{u},\mathbf{u}} & h\mathbb{D}_{\mathbf{u},\omega} & \mathbf{0} \\ h\mathbb{D}_{\mathbf{u},\omega}^T & h^2\mathbb{M}_{\omega,\omega} & h^2\mathbb{M}_{\Gamma} \\ \mathbf{0} & h^2\mathbb{M}_{\Gamma}^T & h^2\mathbb{M}_{p,p} \end{pmatrix}, \tag{46}$$

where $\mathbb{M}_{\mathbf{u},\mathbf{u}}$, $\mathbb{M}_{\omega,\omega}$, and $\mathbb{M}_{p,p}$ are unscaled mass matrices, \mathbb{M}_{Γ} is the unscaled ‘boundary’ mass matrix acting only on boundary degrees of freedom, and $\mathbb{D}_{\mathbf{u},\omega}$ is unscaled ‘difference’ matrix. The structure of $\tilde{\mathbb{K}}$ indicates that reduction of its condition number may be possible by balancing the equations through the diagonal preconditioner

$$\mathbb{D}_p = \begin{pmatrix} h^p \mathbb{I} & \mathbf{0} & \mathbf{0} \\ \mathbf{0} & \mathbb{I} & \mathbf{0} \\ \mathbf{0} & \mathbf{0} & \mathbb{I} \end{pmatrix}, \tag{47}$$

where p is a suitable parameter. Figure 1 shows numerical estimate of the condition number of $\mathbb{D}_p^{1/2} \tilde{\mathbb{K}} \mathbb{D}_p^{1/2}$ as function of p . The smallest condition number is achieved when $p = 3$. Our computational studies confirm that this value also extends to \mathbb{K} , and thus the preconditioned system becomes

$$\mathbb{K}_{\text{prec}} = \mathbb{D}_3^{1/2} \mathbb{K} \mathbb{D}_3^{1/2}. \tag{48}$$

Remark 6

A similar diagonal preconditioner can be used for the dS-VP formulation (24), and in this case, we observed similar improvements in condition number.

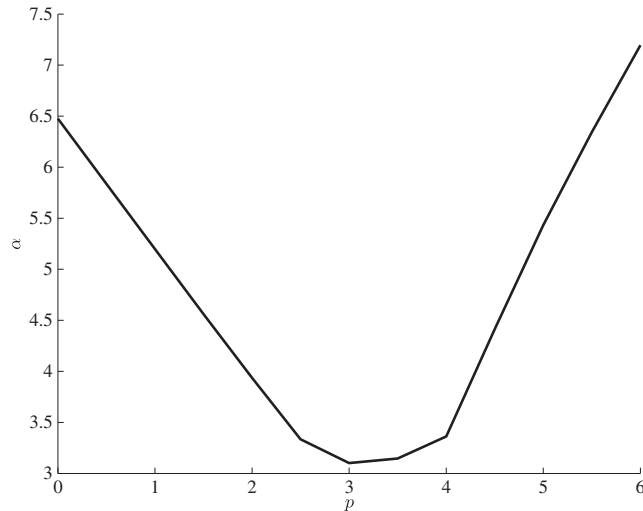


Figure 1. Growth in condition number $O(h^{-\alpha})$ of the preconditioned approximate matrix $\mathbb{D}_p^{1/2} \widetilde{\mathbb{K}} \mathbb{D}_p^{1/2}$ as function of p .

4. EXTENSION TO THE NAVIER–STOKES EQUATIONS

This section extends the dV-VP formulation (32) to the time-dependent Navier–Stokes equations

$$\begin{aligned}
 \frac{\partial \mathbf{u}}{\partial t} - \nu \Delta \mathbf{u} + (\mathbf{u} \cdot \nabla) \mathbf{u} + \nabla p &= \mathbf{f} && \text{for } (\mathbf{x}, t) \in \Omega \times (0, T] \\
 \nabla \cdot \mathbf{u} &= 0 && \text{for } (\mathbf{x}, t) \in \Omega \times (0, T] \\
 \mathbf{u}(\mathbf{x}, 0) &= \mathbf{u}_0(\mathbf{x}) && \text{for } \mathbf{x} \in \Omega,
 \end{aligned} \tag{49}$$

where $\mathbf{u}_0(\cdot)$ denotes the initial velocity field and ν is the kinematic viscosity. The system (49) is augmented with the velocity boundary condition (14) and the zero mean pressure constraint (15). Using the vector identity

$$(\mathbf{u} \cdot \nabla) \mathbf{u} = \frac{1}{2} \nabla |\mathbf{u}|^2 - \mathbf{u} \times \nabla \times \mathbf{u} = \frac{1}{2} \nabla |\mathbf{u}|^2 + \boldsymbol{\omega} \times \mathbf{u}$$

and setting $s = p + 1/2|\mathbf{u}|^2$ to be the total pressure head yields the VVP form of the governing equations

$$\begin{aligned}
 \frac{\partial \mathbf{u}}{\partial t} + \nu \nabla \times \boldsymbol{\omega} + \boldsymbol{\omega} \times \mathbf{u} + \nabla s &= \mathbf{f} && \text{for } (\mathbf{x}, t) \in \Omega \times (0, T] \\
 \nabla \times \mathbf{u} - \boldsymbol{\omega} &= 0 && \text{for } (\mathbf{x}, t) \in \Omega \times (0, T] \\
 \nabla \cdot \mathbf{u} &= 0 && \text{for } (\mathbf{x}, t) \in \Omega \times (0, T] \\
 \mathbf{u}(\mathbf{x}, 0) &= \mathbf{u}_0(\mathbf{x}) && \text{for } \mathbf{x} \in \Omega.
 \end{aligned} \tag{50}$$

To extend the dV-VP formulation (32) to (50), we apply the *finite-difference* LSFEM (FD-LSFEM) approach in [5, Chapter 9]. This approach first discretizes the time derivative by using a finite-difference scheme and then forms a least-squares functional for the resulting semi-discrete in time equations. Because of the limited space, we only present the backward Euler scheme and refer to [5, Chapter 9] for examples of FD-LSFEMs using second-order in time and two-step backward differentiation schemes.

Let $\{[t_{k-1}, t_k]\}_{k=1}^K$ be partition of the time interval $[0, T]$ into K subintervals, where $t_0 = 0$, $t_K = T$, $t_{k-1} < t_k$, and $\tau_k = t_k - t_{k-1}$ for $k = 1, \dots, K$ is the time step. For the backward Euler

method for discretization in time, the sequence of semi-discrete in time systems is given by the following: For $k = 1, \dots, K$,

$$\begin{aligned}
 \frac{1}{\tau_k} \mathbf{u}^{(k)} + \nu \nabla \times \omega^{(k)} + \omega^{(k)} \times \mathbf{u}^{(k)} + \nabla s^{(k)} &= \mathbf{f}(\mathbf{x}, t_k) + \frac{1}{\tau_k} \mathbf{u}^{(k-1)} && \text{in } \Omega \\
 \nabla \times \mathbf{u}^{(k)} - \omega^{(k)} &= 0 && \text{in } \Omega \\
 \nabla \cdot \mathbf{u}^{(k)} &= 0 && \text{in } \Omega \\
 \mathbf{u}^{(k)} &= 0 && \text{on } \Gamma \\
 \int_{\Omega} s^{(k)} \, d\Omega &= 0 \quad ,
 \end{aligned} \tag{51}$$

where $\mathbf{u}^{(0)} = u_0(\mathbf{x})$. Each member of this sequence is a perturbed steady-state Navier–Stokes equation. We apply a least-squares minimization principle to every member of the sequence, which yields a least-squares functional for the Navier–Stokes equations that is well posed in the same function spaces as a least-squares functional for the linear Stokes equations [29]. Therefore, for every k , we have the following counterpart of (16):

$$\begin{aligned}
 J_{-1}^k \left(\mathbf{u}^{(k)}, \omega^{(k)}, s^{(k)}; \mathbf{f}(\mathbf{x}, t_k), \mathbf{u}^{(k-1)} \right) &= \\
 \frac{T}{\nu} \left\| \frac{1}{\tau_k} \mathbf{u}^{(k)} + \nu \nabla \times \omega^{(k)} + \omega^{(k)} \times \mathbf{u}^{(k)} + \nabla s^{(k)} - \mathbf{f}(\cdot, t_k) - \frac{1}{\tau_k} \mathbf{u}^{(k-1)} \right\|_{-1}^2 & \\
 + \|\nabla \times \mathbf{u}^{(k)} - \omega^{(k)}\|_0^2 + \|\nabla \cdot \mathbf{u}^{(k)}\|_0^2 &
 \end{aligned} \tag{52}$$

where $\mathbf{u}^{(0)} = \mathbf{u}_0$. Each problem in the sequence is well posed on the same space as (16), that is, we seek the minimizer $\{\mathbf{u}^{(k)}, \omega^{(k)}, s^{(k)}\}$ out of the space $X = \mathbf{H}_0^1(\Omega) \times L^2(\Omega) \times L_0^2(\Omega)$. Note that on the right-hand side of (52), the weight in the first term is introduced so that all three terms have the same units.

Following the stages in Section 3, we obtain the FD-LSFEM formulation of the dV-VP method for the Navier–Stokes equations:

$$\begin{aligned}
 \tilde{J}_h^{V,k} \left(\mathbf{u}^{(k)}, \omega^{(k)}, s^{(k)}; \mathbf{f}(\mathbf{x}, t_k), \mathbf{u}^{(k-1)} \right) &= \\
 \frac{T}{\nu} \left\| \frac{1}{\tau_k} \mathbf{u}^{(k)} + \nu \nabla \times \omega^{(k)} + \omega^{(k)} \times \mathbf{u}^{(k)} + \nabla s^{(k)} - \mathbf{f}(\cdot, t_k) - \frac{1}{\tau_k} \mathbf{u}^{(k-1)} \right\|_{(h)}^2 & \\
 + \sum_{\kappa \in \mathcal{K}_h(\Omega)} \|\nabla \times \mathbf{u}_h^{(k)} - \omega_h^{(k)}\|_{0,\kappa}^2 + \sum_{\varepsilon \in \mathcal{E}_{h,0}} h^{-3} \left\| [\mathbf{u}_h^{(k)}] \right\|_{0,\varepsilon}^2 + \sum_{\varepsilon \in \mathcal{E}_{h,\Gamma}} h^{-3} \|\mathbf{u}_h^{(k)}\|_{0,\varepsilon}^2 . &
 \end{aligned} \tag{53}$$

Extension of the stream-function modification to (53) is straightforward. For every k , we minimize (53) over the locally solenoidal space (28) or its equal-order counterpart (29).

The first-order optimality condition for (53) is a nonlinear system of algebraic equations. To solve this system, we use the Newton linearization in conjunction with a continuation with respect to the Reynolds number and a preconditioned conjugate gradient method. Because this solution approach does not differ in significant ways from that for a conventional C^0 functional, we skip the details and refer instead to [5, Chapter 8] and the references therein.

5. COMPUTATIONAL STUDY

In this section, we examine the computational properties of the proposed dV-VP least-squares method presented in the previous sections. We implement the method using the equal-order space (29) with $r = 2$. Specifically, we study numerically the conservation of mass in the method, the convergence rates for the method, and the effectiveness of the proposed preconditioner. The C^0 least-squares formulation (5) provides a benchmark against which we assess improvements in the mass conservation and the rates of convergence.

5.1. Conservation of mass

In this section, we examine several aspects of the mass conservation properties of the dV-VP formulation. First, we demonstrate the importance of the proper weight selection in (32). Then we compare (32) with the modified functional (42) and show that the implicit stream-function modification yields additional improvement in the conservation of mass. For convenience, the section provides a brief summary of the test problems used in the studies and explains the method used to evaluate the mass conservation of various LSFEMs.

5.1.1. Test problems. We study mass conservation properties of various LSFEMs using the following test problems: the backward-facing step flow (Figure 2), a channel flow past a cylinder (Figure 3), a split channel flow (Figure 4), and a restricted channel flow (Figure 5). In order to keep the mass loss computations comparable between test domains, each mesh is well refined and generated by using an average element size of $h \approx 0.03$ – 0.04 .

Test problem 1 (Backward-facing step)

For the backward-facing step, the computational domain Ω is the rectangle $[0, 10] \times [0, 1]$ with a re-entrant corner at $(2, 0.5)$. The velocity boundary conditions on the inflow ($x = 0$), outflow ($x = 10$), and horizontal walls are given by

$$\mathbf{u}_{\text{in}} = \begin{bmatrix} 8(y - 0.5)(1 - y) \\ 0 \end{bmatrix}, \mathbf{u}_{\text{out}} = \begin{bmatrix} y(1 - y) \\ 0 \end{bmatrix}, \text{ and } \mathbf{u}_{\text{wall}} = \mathbf{0}, \quad (54)$$

respectively. For this problem, we use \mathcal{K}_h composed of 6442 triangles.

Test problem 2 (Cylinder)

The computational domain Ω for the cylinder problem is the rectangle $[-1, 3] \times [-1, 1]$ with a disk-shaped obstacle of radius $r > 0$ centered at $(0, 0)$. The difficulty of this test increases as the radius reduces the size of the gap above and below the disk. In our example, we use $r = 0.9$. The velocity boundary conditions on the inflow ($x = -1$), outflow ($x = 3$), top ($y = 1$), and bottom ($y = -1$) walls are given by

$$\mathbf{u}_{\text{in}} = \mathbf{u}_{\text{out}} = \mathbf{u}_{\text{wall}} = \begin{bmatrix} (1 - y)(1 + y) \\ 0 \end{bmatrix}, \quad (55)$$

whereas on the surface of the cylinder, we impose $\mathbf{u}_{\text{cyl}} = \mathbf{0}$. We solve this test problem on \mathcal{K}_h with 6011 triangles.

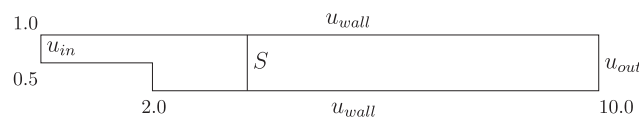


Figure 2. Geometry of test problem 1: backward-facing step.

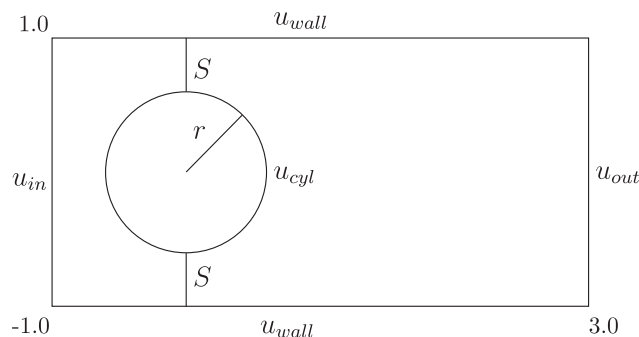


Figure 3. Geometry of test problem 2: flow past a cylinder.

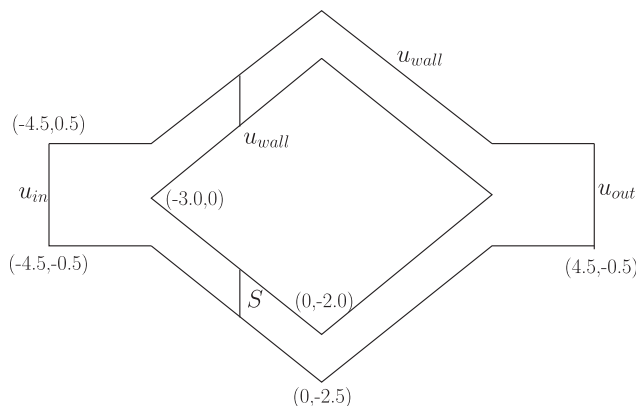


Figure 4. Geometry of test problem 3: split channel.

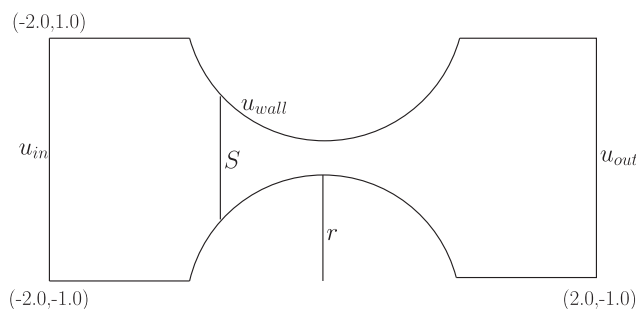


Figure 5. Geometry of test problem 4: restricted channel.

Test problem 3 (Split channel)

In this example, we model channel flow split into two separate channels and then finally combining back into a single channel. The computational domain begins with a height of 1 and splits off into two channels of height 0.5. For the boundary conditions, we set

$$\mathbf{u}_{in} = \mathbf{u}_{out} = \begin{bmatrix} (0.5 - y)(0.5 + y) \\ 0 \end{bmatrix}, \text{ and } \mathbf{u}_{wall} = \mathbf{0}. \tag{56}$$

This test problem is solved on \mathcal{K}_h with 6694 triangles.

Test problem 4 (Restricted channel)

For the restricted channel domain, we have a channel flow that is pinched in on the top and bottom sides. The domain is the rectangular domain $[-2, 2] \times [-1, 1]$. The channel is pinched in at $x = 0$ using two semi-cylindrical cut outs of radius r . Similar to the cylinder flow domain, the larger the radius, the more narrow the opening of the channel and hence increasing the difficulty of the problem. In our examples, we use $r = 0.9$. The boundary conditions are set as in (55), and the domain is meshed using 4124 triangles.

In each of the test problems, the boundary conditions are compatible with $\nabla \cdot \mathbf{u} = 0$. To assess mass conservation, we follow the procedure from [1] modified to account for the weak imposition of the boundary conditions in (32) and (42). Specifically, we measure the total mass flow across a sequence of vertical surfaces connecting the top and bottom sides of the computational domain and the parts of the domain boundary between Γ_{in} and these surfaces. The lines denoted by S in Figures 2–5 show examples of such surfaces.

As $\mathbf{u} = \mathbf{0}$ on all parts of $\partial\Omega$ except Γ_{in} and Γ_{out} in each test problem, the divergence theorem implies

$$\int_{\Gamma_{\text{in}}} \mathbf{u} \cdot \mathbf{n}_{\text{in}} \, d\ell = \int_S \mathbf{u} \cdot \mathbf{n}_S \, d\ell, \quad (57)$$

for any S connecting the top and bottom walls of the domain. However, because the boundary condition is imposed weakly, $\mathbf{u}_h \approx 0$ on these parts of the boundary. Therefore, we quantify the percent mass loss across the surface S and the boundary of $\partial\Omega$ extending from Γ_{in} to S , which we denote by Γ_S :

$$\%m_{\text{loss}} = \frac{\int_{\Gamma_{\text{in}}} \mathbf{u} \cdot \mathbf{n}_{\text{in}} \, d\ell - \left(\int_{\Gamma_S} \mathbf{u} \cdot \mathbf{n}_{\Gamma_S} \, d\ell + \int_S \mathbf{u} \cdot \mathbf{n}_S \, d\ell \right)}{\int_{\Gamma_{\text{in}}} \mathbf{u} \cdot \mathbf{n}_{\text{in}} \, d\ell} \times 100. \quad (58)$$

Because the velocity basis is locally divergence free on each element, the finite element solution always satisfies $\|\nabla \cdot \mathbf{u}_h\| = 0$. For this reason, we do not use the $H(\text{div})$ semi-norm to assess the quality of the mass conservation.

5.1.2. The role of the proper velocity jump weighting. To demonstrate the importance of setting the velocity jump weight in (32) equal to h^{-3} , we solve the four test problems by using three different weights for this term in (30). Our implementation uses the equal-order space (29) with $r = 2$. We set $\|\cdot\|_{(h)} = h\|\cdot\|_0$ and choose $\alpha = -1, -2, -3$. The C^0 least-squares solution of (20), implemented with the equal-order space $X_h^{(2)}$, provides the benchmark. The plots in Figure 6 summarize the numerical results for the four examples. In particular, the mass loss data show that when using the correct weight on the jump term, (30) performs very well—that is, the maximum mass loss in each test problem is less than 1% at 0.17%, 0.95%, 0.70%, and 0.88% for each test problem, respectively. On the other hand, the results also indicate that if the changes in the scaling of the least-squares terms induced by the piecewise solenoidal velocity space (11) are not taken into consideration, conservation of mass suffers. Specifically, if the weight of the velocity jump is left at h^{-1} , as in the dS-VP functional (24), then the peak mass loss in all four test problems is similar to the C^0 solution.

5.1.3. The role of the implicit stream-function modification. To demonstrate the impact of (39) on the conservation of mass, we solve the test problems using both (32) and (42), implemented with the equal-order space (29), and $r = 2$. Figure 7 shows that inclusion of (39) reduces the mass loss from 0.17%, 0.95%, 0.70%, and 0.88% to 0.04%, 0.27%, 0.18%, and 0.13% for each of the test problems, respectively. When compared with (32), this is a reduction in mass loss by a factor of approximately 4 for each test problem.

The results presented so far confirm that (32) and (42) offer significant improvements in the conservation of mass, compared with standard C^0 least-squares methods. The scale of these improvements is such that the solutions of (32) and (42) on the one hand, and the C^0 LSFEM (18) on the other hand, exhibit visible qualitative differences. To conclude this section, we present several solution plots that demonstrate these differences.

In Figures 8–11, the velocity field is plotted for (18) and (42) with colors representing the magnitude of the vector field. For the backward step, Figure 8 shows that the magnitude of the velocity field in the C^0 formulation decreases as the flow reaches the re-entrant corner at $x = 2$; whereas for (42), the initial velocity profile is propagated until the re-entrant corner. For the second test problem, the difference in intensities of the velocity profile at $x = 0$ is clear with a maximum velocity of almost 10.0 in (42) compared with only 5.0 for (18). In the split channel domain, an initial channel of height 1.0 is split into two channels of height 0.5. Although the height of the two split channels are 0.5, the diameter of the opening is less because of the angle of the split. The velocity profile for (42) demonstrates an increase in velocity in the channels with the velocity profile being propagated through the channels. In the C^0 solution, the magnitude of the velocity does not increase relative

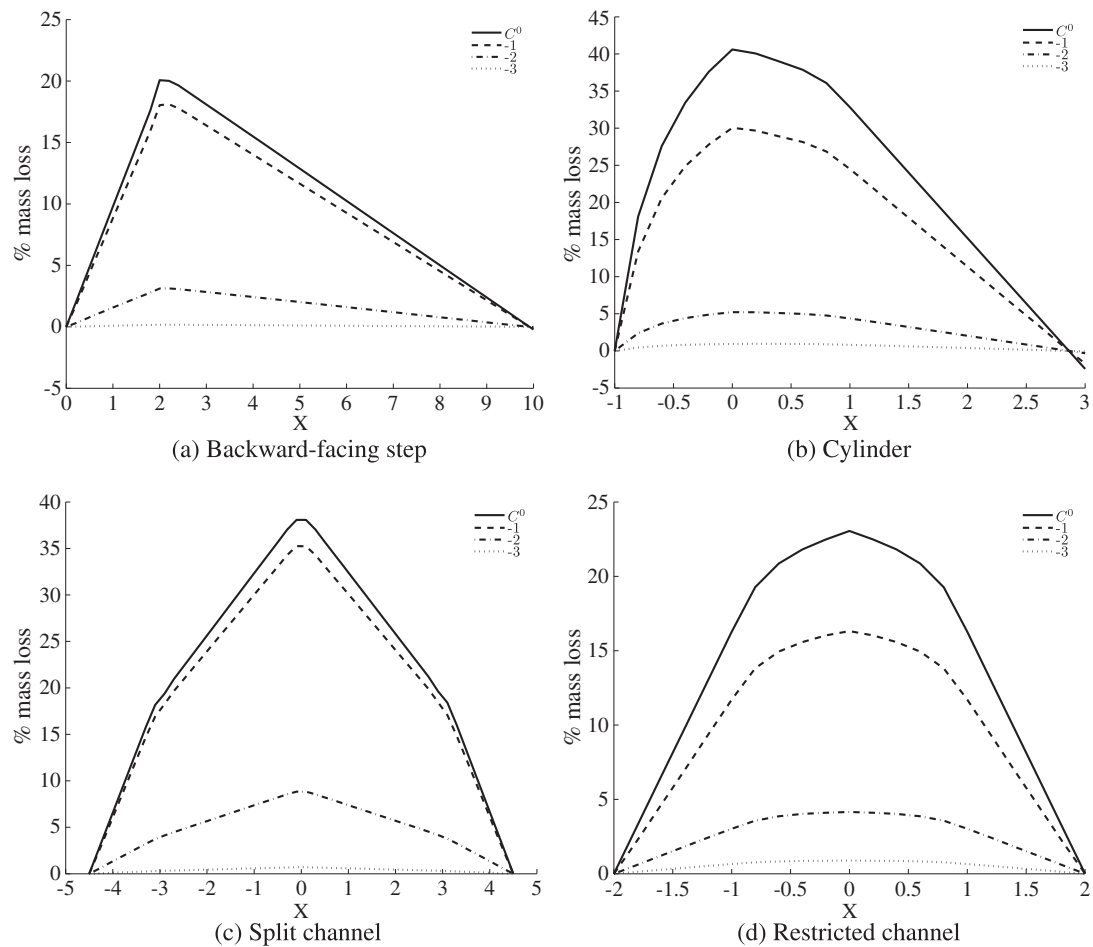


Figure 6. Comparison of the mass loss in the discontinuous velocity LSFEM (30) with $\|\cdot\|_h = h\|\cdot\|_0$, and $\alpha = -1, -2, -3$ versus standard C^0 LSFEM (18).

to the initial velocity, and additionally, the magnitude of the velocity dissipates within each of the split channels. The behavior in the restricted channel domain is similar to that of the cylinder flow problem with (42) pushing twice as much flow as (18) at the narrowest part of the opening.

5.2. Convergence

In this section, we compare convergence rates of the dV-VP LSFEM with and without the integral jump term. The computational domain Ω is the unit square. \mathcal{K}_h is uniform partition of Ω into square elements with side length equal to $h_i = 2^{-i}$ for $i = 1, 2, 3, 4, 5$. The convergence rates are estimated using a manufactured solution, where the exact solution is selected as

$$\mathbf{u} = \begin{bmatrix} -\pi \sin(\pi y) \\ \pi \sin(\pi x) \end{bmatrix}, \quad \omega = \nabla \times \mathbf{u} = \pi^2(\cos(\pi x) + \cos(\pi y)), \quad p = \sin(x) \exp(y),$$

and hence, the corresponding right-hand side is

$$\mathbf{f} = \begin{bmatrix} -\pi^3 \sin(\pi y) + \cos(x) \exp(y) \\ \pi^3 \sin(\pi x) + \sin(x) \exp(y) \end{bmatrix}.$$

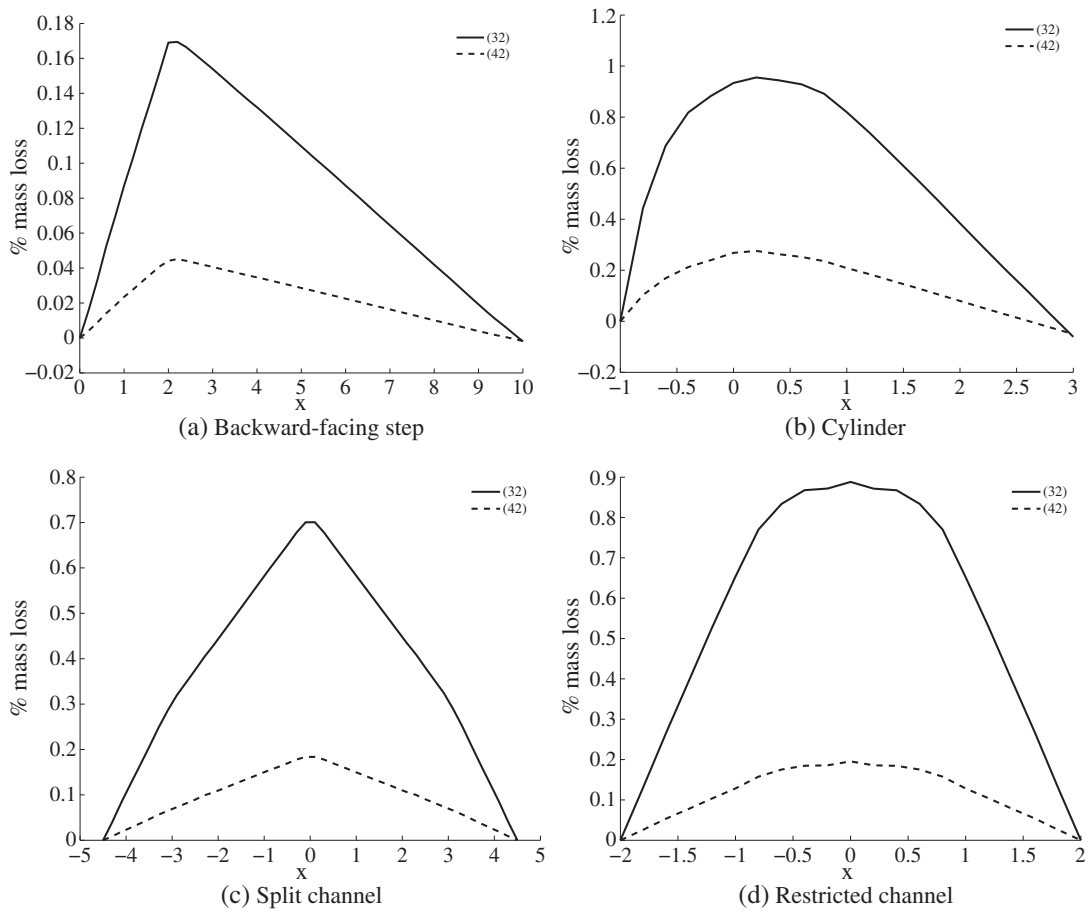


Figure 7. Comparison of the mass loss in the discontinuous velocity LSFEM with $\|\cdot\|_{(h)} = h\|\cdot\|_0$, with (42) versus without (32) the implicit stream-function term.

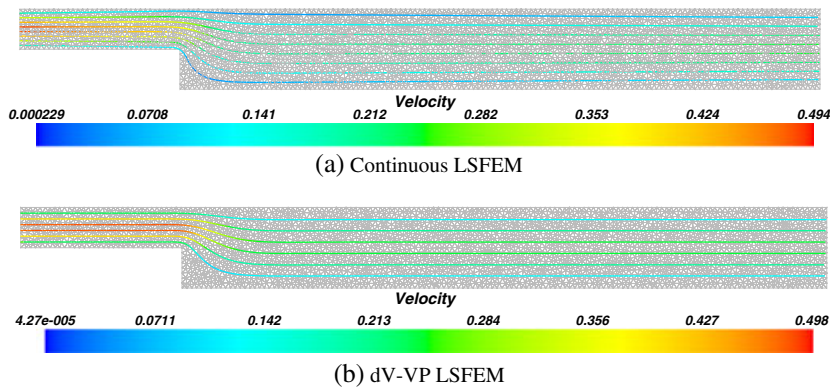
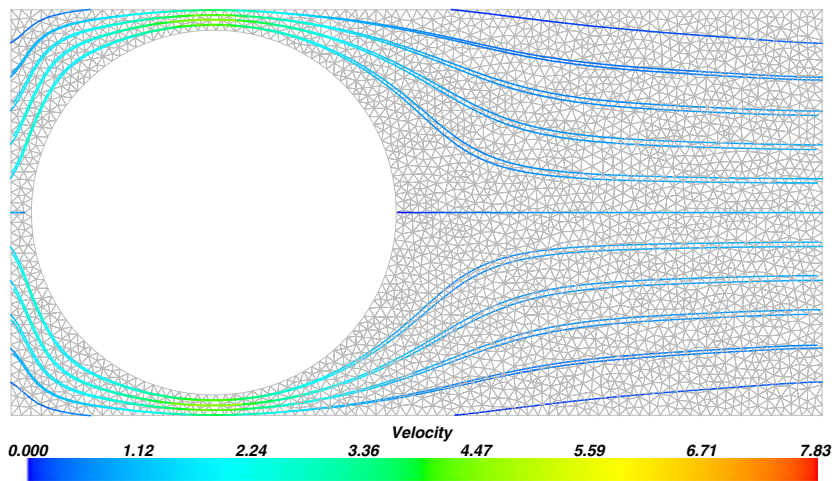


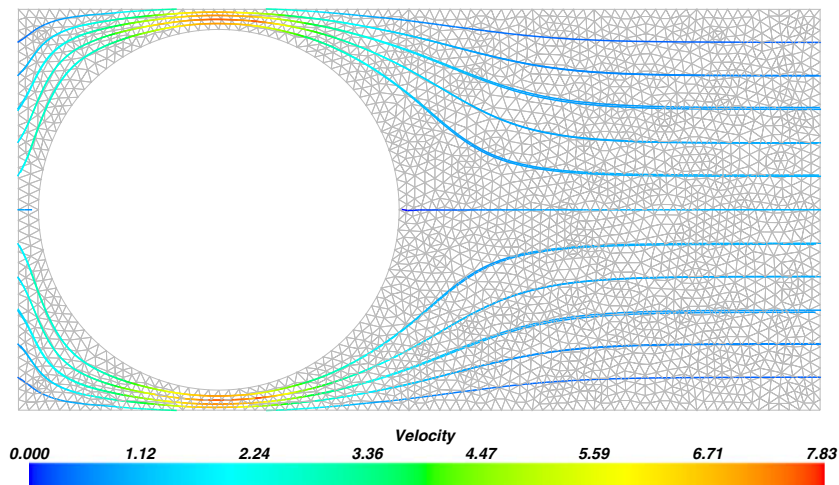
Figure 8. Velocity plot of (5) and (42) on the backward step domain, Test problem 1.

Tables I–III demonstrate that the method indeed exhibits the optimal convergence rates as expected from Theorem 1. However, because the vorticity and pressure are implemented using quadratic basis functions, we observe that

$$\|\omega - \omega^h\|_0 = \|p - p^h\|_0 = O(h^3) \quad \text{and} \quad \|\omega - \omega^h\|_1 = \|p - p^h\|_1 = O(h^2), \quad (59)$$



(a) Continuous LSFEM



(b) dV-VP LSFEM

Figure 9. Velocity plot of (5) and (42) on the cylinder flow domain, Test problem 2.

which is expected for quadratic basis functions. Furthermore, it can be seen that the inclusion of the jump term enforcing the continuity of the implicit stream function, which improved the mass conservation as demonstrated in Section 3, does not affect the convergence rates of the method.

5.3. Preconditioning

We next study the effectiveness of the preconditioner in (48). We estimate numerically the growth in condition number of the matrix as the mesh is refined for formulations before and after the application of the preconditioners.

Table IV demonstrates that without a preconditioner, the growth in condition number of (42) as the mesh is refined is approximately $O(h^{-6})$. The preconditioner (48) reduces the growth in the condition number by a factor of 2. In both cases, the growth in the condition number is in line with the numerical estimates in Figure 1. As a point of reference, the dependence on h is $O(h^{-4})$ and $O(h^{-2})$ for (18) and (19), respectively; see [5, Theorem 4.8, p.119] and [5, Theorem 4.10, p.126]. Therefore, preconditioner (48) reduces the growth in condition number close to that of the discrete negative norm.

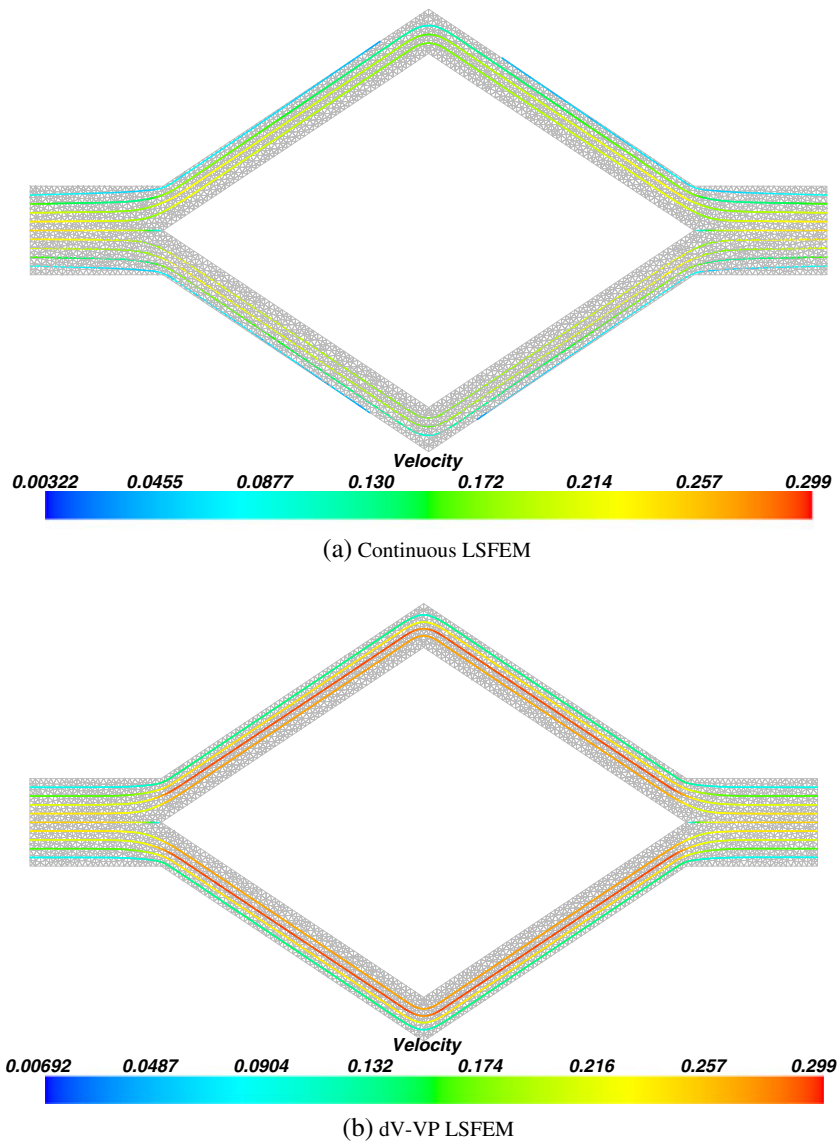


Figure 10. Velocity plot of (5) and (42) on the split channel domain, Test problem 3.

5.4. Comparison with a mixed Galerkin method

This section compares the dV-VP formulation (42) with the mixed Galerkin finite element for the Stokes equations implemented using the classical TH element pair. We recall that the TH element is composed of continuous, piecewise quadratic elements for the velocity and continuous, piecewise linear elements for the pressure. It is well known that the TH element satisfies the inf-sup condition necessary for the stability of the mixed method. The asymptotic accuracy of the velocity in the TH element matches that of the divergence-free space used in the implementation of (40).

A comprehensive comparison of the two methods is beyond the scope of this paper. Thus, we limit our study to the conservation of mass for the backward-facing step (Test problem 1), the cylinder (Test problem 2), and the restricted channel (Test problem 4) test problems. We use the same grids as in the previous section, that is, we solve the mixed Galerkin formulation for each test problem on grids having 6442, 6011, and 4124 elements, respectively. The linear systems are solved using preconditioned GMRES, and the tolerance is set to the same value as in the preconditioned conjugate gradients used to solve the dV-VP linear systems. The velocity boundary condition in the mixed

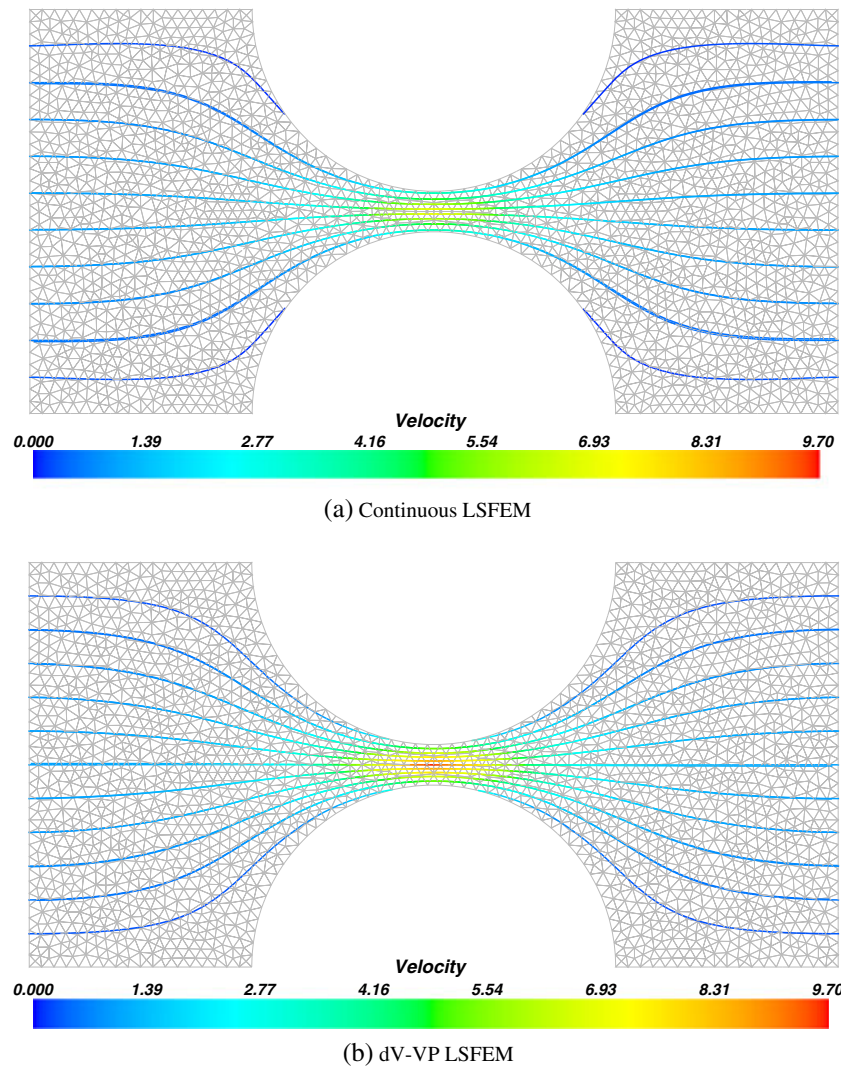


Figure 11. Velocity plot of (5) and (42) on the restricted channel domain, Test problem 4.

Galerkin method is imposed strongly by specifying the nodal values of the velocity at all boundary nodes. The strong imposition of the velocity boundary condition simplifies the mass loss formula (58) to

$$\%m_{\text{loss}} = \frac{\int_{\Gamma_{\text{in}}} \mathbf{u} \cdot \mathbf{n}_{\text{in}} \, d\ell - \int_{\Gamma_S} \mathbf{u} \cdot \mathbf{n}_{\Gamma_S} \, d\ell}{\int_{\Gamma_{\text{in}}} \mathbf{u} \cdot \mathbf{n}_{\text{in}} \, d\ell} \times 100.$$

The plots in Figure 12 present the mass loss data for the three test problems. In all three cases, the dV-VP formulation clearly outperforms the mixed Galerkin formulation. In particular, we see that for the cylinder flow, the mass loss using the TH pair can be as high as 13%. Although the mass loss in the mixed method is below 2% in the other two cases, it is still significantly higher than the mass loss in the dV-VP method.

It is worth pointing out that the TH solution experiences rapid loss of mass in a narrow boundary layer adjacent to the inflow boundary and then gradually recovers the lost mass. This behavior is distinctly different from the pattern of the mass loss in the least-squares method and certainly merits

Table I. Convergence rates of velocity \mathbf{u} , for (32) and (42).

LSFEM	$\widehat{J}_{(h)}^V$ (32)				$\widetilde{J}_{(h)}^V$ (42)			
	$\ \mathbf{u} - \mathbf{u}_h\ _0$	Rate	$\ \mathbf{u} - \mathbf{u}_h\ _1$	Rate	$\ \mathbf{u} - \mathbf{u}_h\ _0$	Rate	$\ \mathbf{u} - \mathbf{u}_h\ _1$	Rate
1/4	8.118e-3	—	2.274e-1	—	8.116e-3	—	2.274e-1	—
1/8	1.071e-3	2.922	5.680e-2	2.001	1.071e-3	2.922	5.680e-2	2.001
1/16	1.366e-4	2.947	1.419e-2	2.001	1.366e-4	2.946	1.419e-2	2.001
1/32	1.769e-5	2.950	3.547e-3	2.001	1.769e-5	2.950	3.547e-3	2.001
1/64	2.888e-6	2.883	8.868e-4	2.001	2.897e-6	2.883	8.868e-4	2.001

Table II. Convergence rates of vorticity ω , for (32) and (42).

LSFEM	$\widehat{J}_{(h)}^V$ (32)				$\widetilde{J}_{(h)}^V$ (42)			
	$\ \omega - \omega_h\ _0$	Rate	$\ \omega - \omega_h\ _1$	Rate	$\ \omega - \omega_h\ _0$	Rate	$\ \omega - \omega_h\ _1$	Rate
1/4	5.040e-2	—	1.007e0	—	5.026e-2	—	1.006e0	—
1/8	4.562e-3	3.466	2.147e-1	2.230	4.563e-3	3.461	2.147e-1	2.228
1/16	5.874e-4	3.211	5.784e-2	2.061	5.876e-4	3.209	5.785e-2	2.061
1/32	1.016e-4	2.982	1.908e-2	1.906	1.016e-4	2.981	1.908e-2	1.905
1/64	2.847e-5	2.706	7.865e-3	1.750	2.856e-5	2.705	7.866e-3	1.750

Table III. Convergence rates of pressure p , for (32) and (42).

LSFEM	$\widehat{J}_{(h)}^V$ (32)				$\widetilde{J}_{(h)}^V$ (42)			
	$\ p - p_h\ _0$	Rate	$\ p - p_h\ _1$	Rate	$\ p - p_h\ _0$	Rate	$\ p - p_h\ _1$	Rate
1/4	8.320e-2	—	7.349e-1	—	8.292e-2	—	7.331e-1	—
1/8	6.525e-3	3.673	1.088e-1	2.756	6.542e-3	3.664	1.089e-1	2.751
1/16	9.049e-4	3.261	2.325e-2	2.491	9.086e-4	3.256	2.327e-2	2.489
1/32	1.922e-4	2.912	5.603e-3	2.333	1.927e-4	2.910	5.609e-3	2.333
1/64	5.327e-5	2.883	1.399e-3	2.234	5.347e-5	2.628	1.401e-3	2.234

Table IV. Growth in condition number $O(h^{-\alpha})$ for original and preconditioned matrices for (27), (32), and (42).

LSFEM	No preconditioning	With preconditioning
$J_{(h)}^V$	3.9	3.9
$\widehat{J}_{(h)}^V$	5.8	2.9
$\widetilde{J}_{(h)}^V$	5.8	2.8

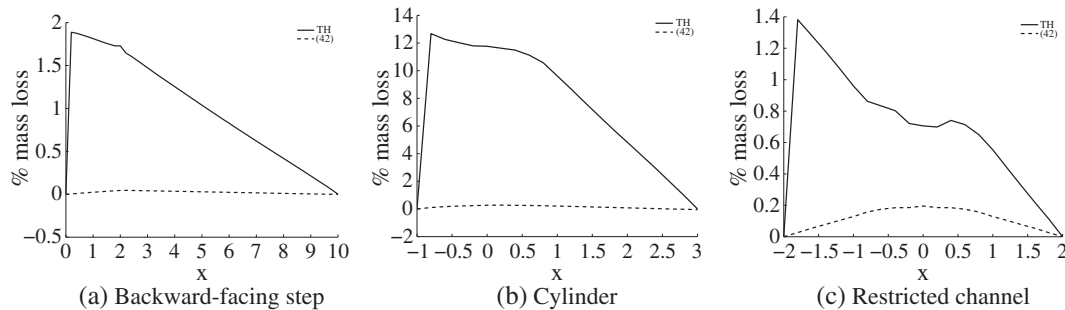


Figure 12. Comparison of the mass loss in the discontinuous velocity LSFEM (42) with $\|\cdot\|_{(h)} = h\|\cdot\|_0$ versus mixed Galerkin formulation of the Stokes problem with the Taylor–Hood element.

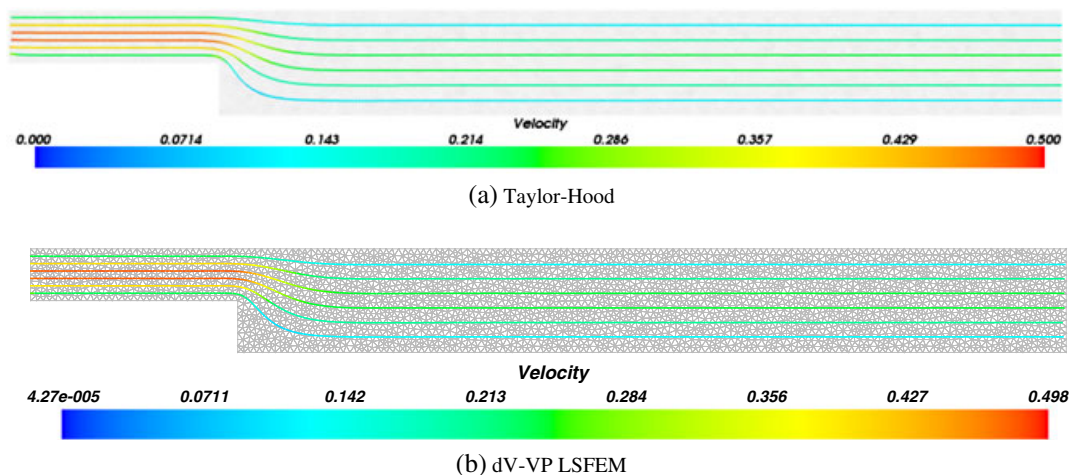


Figure 13. Velocity plot of the mixed Galerkin method and (42) on the backward step domain, Test problem 1.

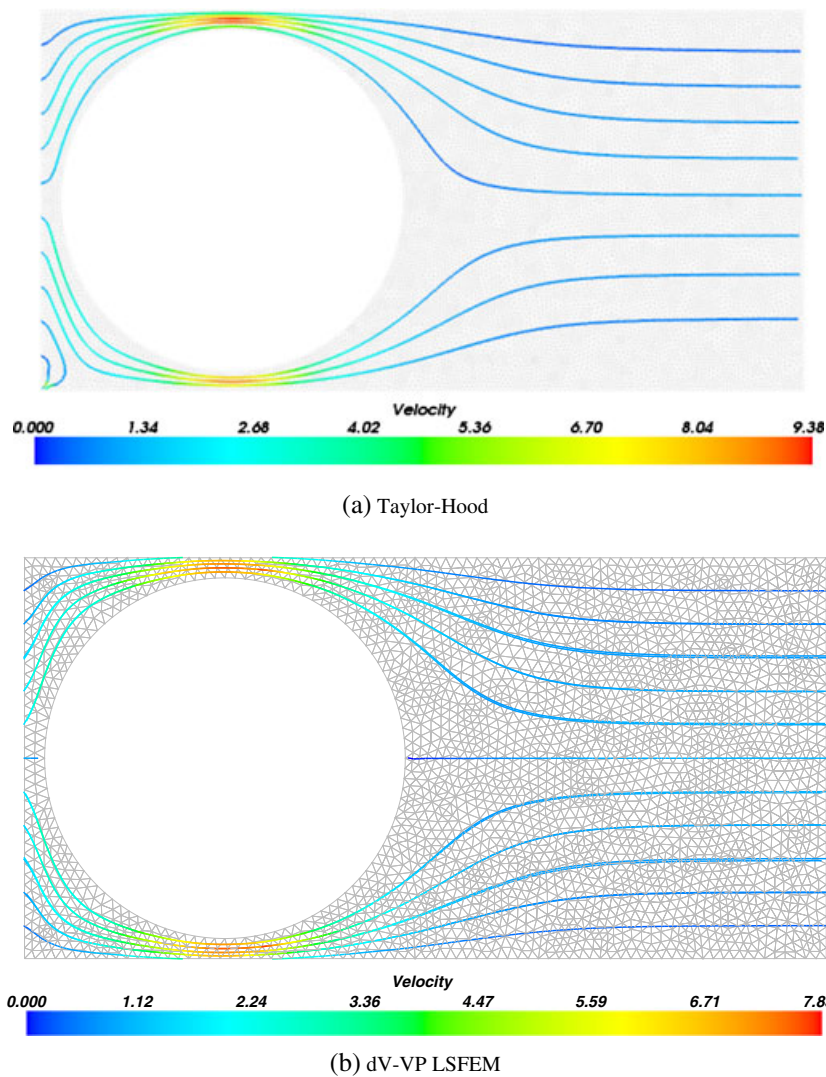
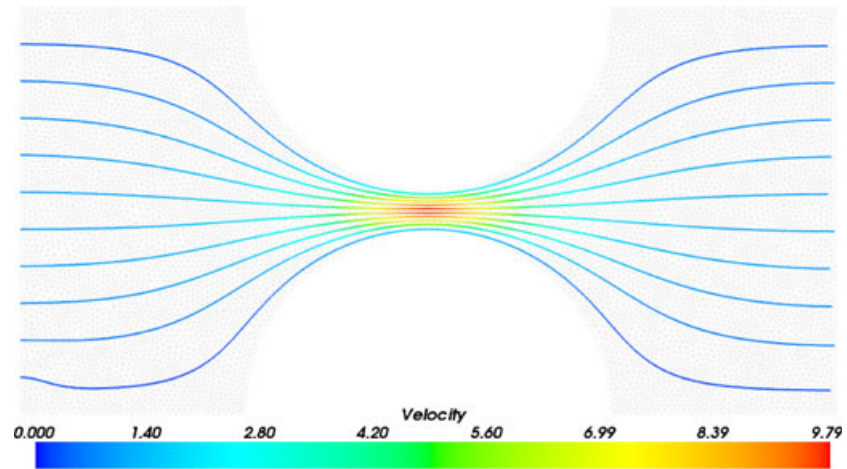
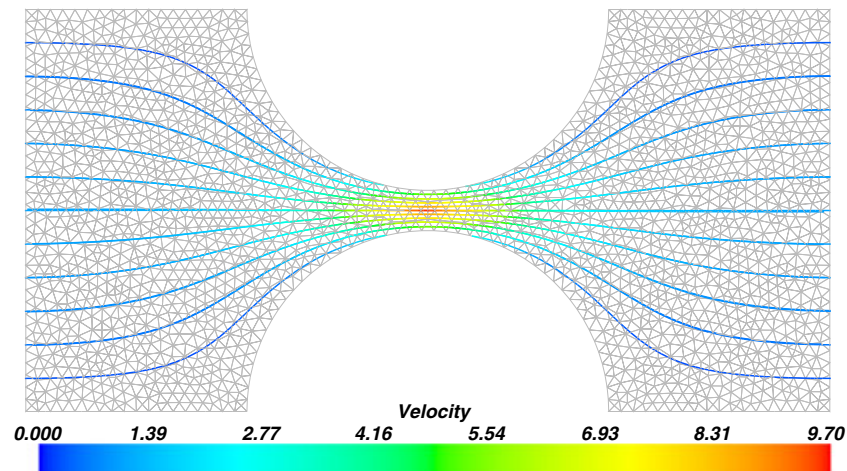


Figure 14. Velocity plot of the mixed Galerkin method and (42) on the cylinder flow domain, Test problem 2.



(a) Taylor-Hood



(b) dV-VP LSFEM

Figure 15. Velocity plot of the mixed Galerkin method and (42) on the restricted channel domain, Test problem 4.

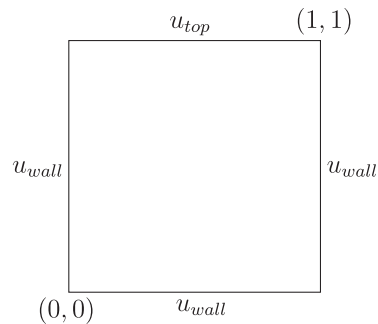


Figure 16. Domain for lid-driven cavity.

further examination. The strong imposition of the velocity boundary condition in the mixed Galerkin method could be a contributing factor to this phenomena. There is some evidence [30] that weakly enforced boundary conditions are better, at least in some flow regimes, than strongly enforced ones. We refer to [31] and the references therein for further information on this subject.

The velocity field plots in Figures 13–15 provide additional information about the quality of the solution by the two methods. Two observations are worth pointing out. For the backward step and the restricted channel flow problems, the strengths of the velocity fields for the dV-VP and the mixed Galerkin method appear very similar, which is consistent with the fact that for these two cases the mass loss in the mixed method is below 2%. However, for the cylinder flow, the velocity plots in Figure 14 do exhibit some qualitative differences. Furthermore, Figures 14 and 15 indicate that the dV-VP formulation does a better job at preserving the symmetry of the flow.

5.5. Navier–Stokes equations

In this section, we present preliminary numerical examples with the dV-VP formulation for the two-dimensional steady-state Navier–Stokes equations. In this case, the functional (53) with the implicit stream-function modification specializes to

$$\begin{aligned} \tilde{J}_h^V(\mathbf{u}, \omega, s; \mathbf{f}) = & \frac{1}{\nu} \|\mathbf{u} + \nu \nabla \times \omega + \omega \times \mathbf{u} + \nabla s - \mathbf{f}\|_{(h)}^2 + \sum_{\kappa \in \mathcal{K}_h(\Omega)} \|\nabla \times \mathbf{u}_h - \omega_h\|_{0,\kappa}^2 \\ & + \sum_{\varepsilon \in \mathcal{E}_{h,0}} \left(h^{-3} \|\llbracket \mathbf{u}_h \rrbracket\|_{0,\varepsilon}^2 + h^{-5} |\varepsilon| \left[\int_{\varepsilon} \mathbf{u}_h \cdot \mathbf{n} \, d\ell \right]^2 \right) + \sum_{\varepsilon \in \mathcal{E}_{h,\Gamma}} h^{-3} \|\mathbf{u}_h\|_{0,\varepsilon}^2. \end{aligned} \quad (60)$$

We solve (60) by using a continuation along the constant strategy in conjunction with the Newton linearization. The solution of the linearized equations is by conjugate gradients preconditioned by (47).

In this section, we implement the preceding method for two commonly used tests problems, the lid-driven cavity and the backward-facing step used in the Stokes calculations (Figure 2).

For the lid-driven cavity problem, the domain is a unit square with a horizontal velocity on the top wall. The lid-driven cavity domain is shown in Figure 16 and is meshed by 6694 triangles. The boundary conditions for the lid-driven cavity domain are given by

$$\mathbf{u}_{\text{top}} = \begin{bmatrix} 1 \\ 0 \end{bmatrix}, \quad \mathbf{u}_{\text{wall}} = \begin{bmatrix} 0 \\ 0 \end{bmatrix}. \quad (61)$$

5.5.1. Backward-facing step. Our first test problem for the Navier–Stokes equations revisits the backward-facing step used to test the dV-VP formulation for the Stokes equations. We implement

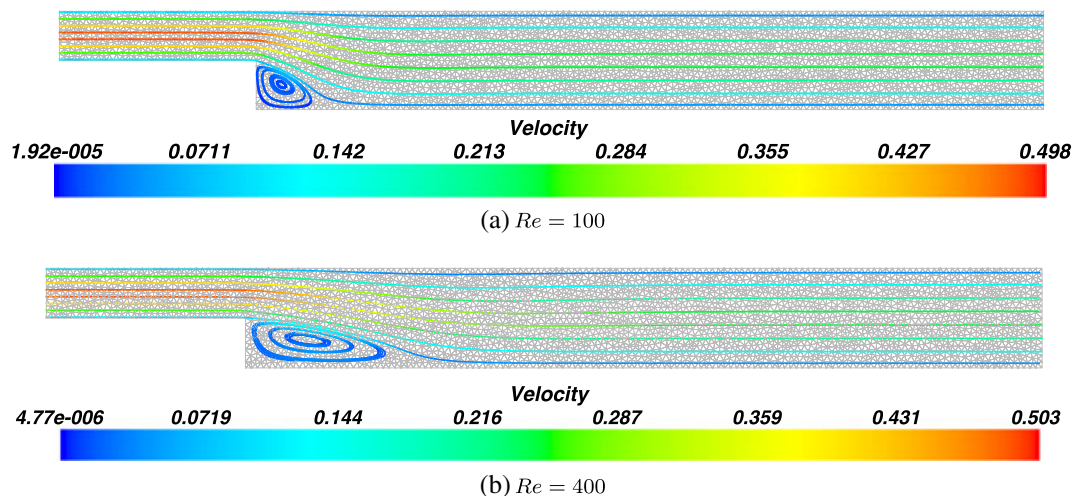


Figure 17. Streamlines for backward-facing step problem with $Re = 100$ (a) and $Re = 400$ (b). Color gradient shows magnitude of velocity.

(60) for the domain and boundary conditions described in Figure 2 and (54), and we solve the equations with Reynolds numbers $Re = 100$ and $Re = 400$. The streamlines for each case are plotted in Figure 17. For $Re = 100$, we see a small vortex forming at the corner of the step interface, which is not evident in the Stokes equations. As the Reynolds number increases to $Re = 400$, we see a larger vortex forming, and the magnitude of the velocity above the vortex is much larger when compared with $Re = 100$ and the standard Stokes equations. The mass loss throughout the domain is summarized in Figure 18. It is clear that the dV-VP method performs extremely well with respect to mass conservation with only 0.11% and 0.05% mass loss for $Re = 100$ and $Re = 400$, respectively.

5.5.2. *Lid-driven cavity.* Upon visual inspection, the streamlines plotted in Figure 19 closely match the results in [32]. For $Re = 100$, the central vortex is in the upper right with two small vortices forming in the bottom left and right corners. For $Re = 400$, the central vortex is shifted towards the center, and the bottom vortices are larger. A more quantitative comparison is shown in Figures 20 and 21 where the values of the velocities are compared on lines through the center of the domain.

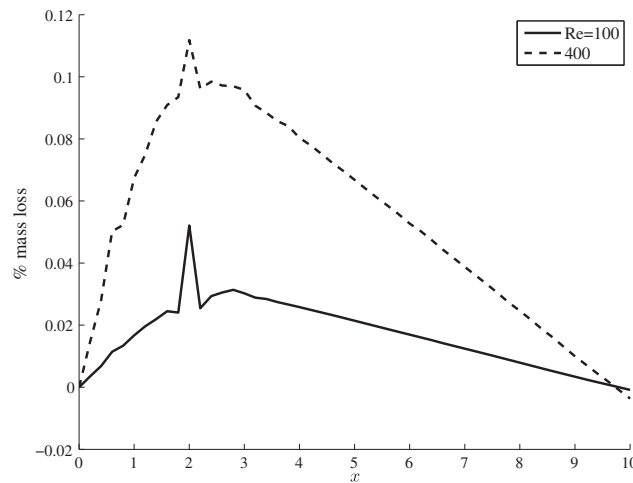


Figure 18. Mass loss for backward-facing step domain for $Re = 100$ and $Re = 400$.

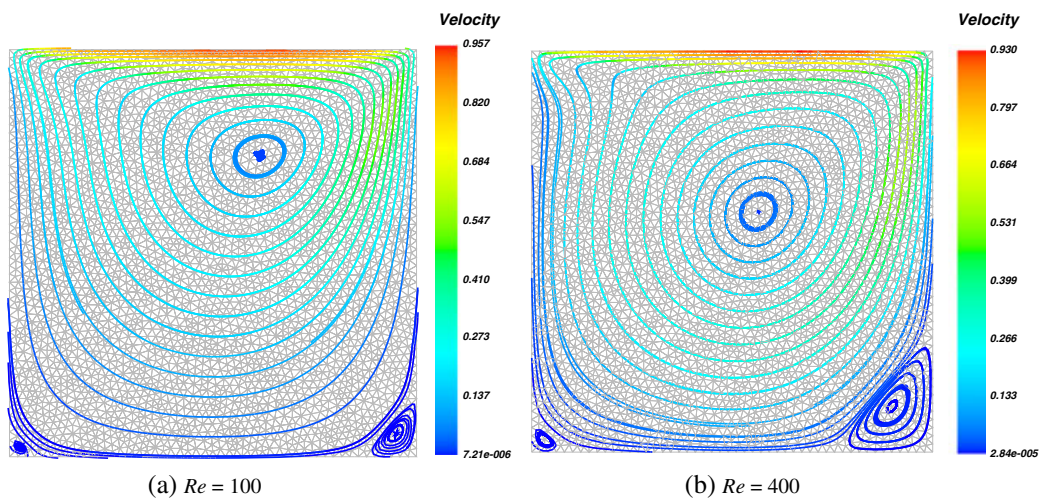


Figure 19. Streamlines for lid-driven cavity with Reynolds number $Re = 100$ (a) and $Re = 400$ (b). Color gradient shows magnitude of velocity.

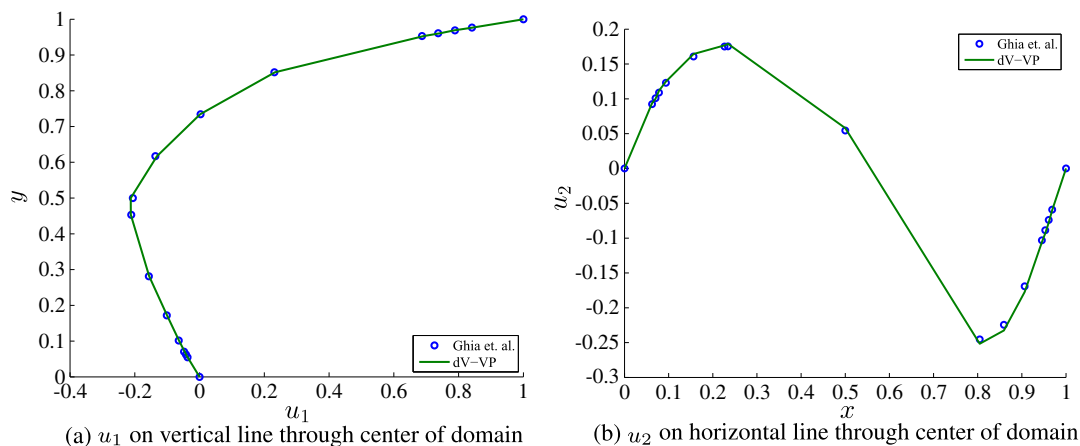


Figure 20. Comparison of dV-VP velocities (solid lines) versus benchmark results [32] (circles) for Reynolds number $Re = 100$.

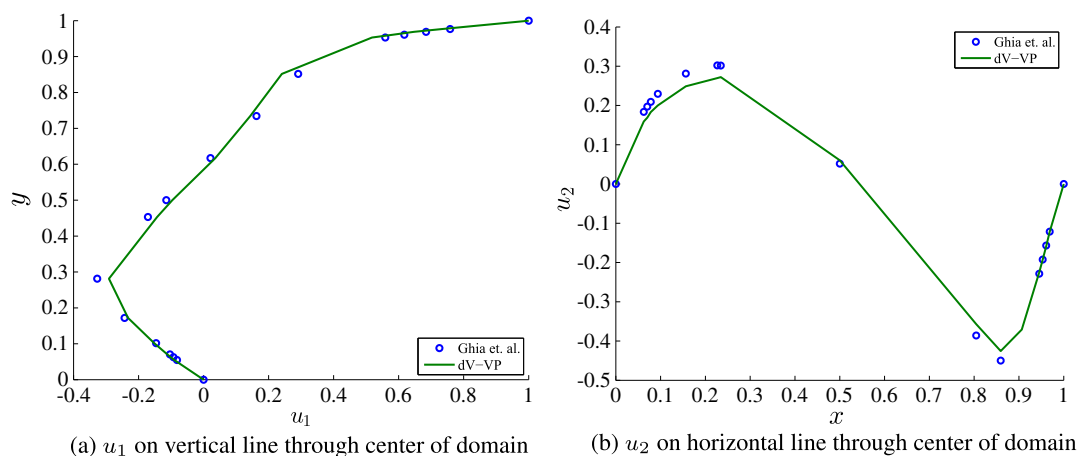


Figure 21. Comparison of dV-VP velocities (solid lines) versus benchmark results [32] (circles) for Reynolds number $Re = 400$.

For Reynolds number $Re = 100$, the dV-VP method recovers the solution of [32] almost exactly. Furthermore, for $Re = 400$, the dV-VP method performs extremely well considering that the mesh size is $h \approx 0.017$, whereas the benchmark results are obtained using 129×129 uniform grid points, that is, $h \approx 0.0078$. Compared with the C^0 LSFEM results found in [5], the dV-VP method dramatically improves least-squares methods for the Navier–Stokes equations.

6. CONCLUSIONS

In this paper, we continue the efforts of [1] to improve mass conservation in least-squares finite elements for incompressible fluid flows, while preserving the most attractive properties of this class of methods. To avoid complications from the use of stream functions, in this paper, we employ a non-conforming piecewise divergence-free basis for the velocity. The resulting dV-VP least-squares formulation does not include second-order derivatives, simplifies the imposition of the velocity boundary condition, and shows high mass conservation. In two dimensions, the dS-VP formulation of [1] prompts a modification of the dV-VP functional, which further reduces the mass losses in the least-squares solution.

The numerical studies in the paper demonstrate that the resulting dV-VP least-squares method has superior mass conservation compared with a standard C^0 least-squares method. These studies also show improved mass conservation relative to the mixed Galerkin method implemented with the TH element pair.

A simple diagonal preconditioner is introduced to reduce the growth in condition number relative to mesh refinement down to levels comparable with Galerkin and discrete negative norm methods.

Finally, we extend the dV-VP formulation to the Navier–Stokes equations. Our preliminary numerical results indicate that the mass conservation properties of the dV-VP LSFEM are fully retained in this setting and that the method compares very well with published benchmark results.

ACKNOWLEDGEMENTS

This work was partially supported by the NSF (contract/grant number DMS 07-46676). This work was also supported by Sandia National Laboratories, a multi-program laboratory operated by Sandia Corporation, a wholly owned subsidiary of Lockheed Martin Corporation, for the US Department of Energy’s National Nuclear Security Administration under contract DE-AC04-94AL85000.

We are grateful to the anonymous referees for the careful and thorough reading of the paper. Their suggestions, comments, and questions helped us to significantly improve the organization, the readability, and the content of the paper. We also thank John Burkhardt and Lili Ju for providing the GMRES solver used for the mixed Galerkin formulation.

REFERENCES

1. Bochev P, Lai J, Olson L. A locally conservative, discontinuous least-squares finite element method for the Stokes equations. *International Journal for Numerical Methods in Fluids* 2012; **68**(6):782–804.
2. Chang CL, Nelson JJ. Least-squares finite element method for the Stokes problem with zero residual of mass conservation. *SIAM Journal on Numerical Analysis* 1997; **34**(2):480–489.
3. Proot MM, Gerritsma MI. Mass- and momentum conservation of the least-squares spectral element method for the Stokes problem. *Journal of Scientific Computing* 2006 June; **27**:389–401.
4. Pontaza JP, Reddy JN. Spectral/hp least-squares finite element formulation for the Navier–Stokes equations. *Journal of Computational Physics* 2003; **190**(2):523–549.
5. Bochev P, Gunzburger M. *Least-Squares Finite Element Methods*, Applied Mathematical Sciences, Vol. 166. Springer Verlag: Berlin, Heidelberg, New York, 2009.
6. Bochev P, Gunzburger M. A locally conservative mimetic least-squares finite element method for the Stokes equations. In *Proceedings of IJSSC 2009*, Vol. 5910, Lirkov I, Margenov S, Wasniewski J (eds), Springer Lecture Notes in Computer Science. Springer: Berlin, Heidelberg, New York, 2009; 637–644.
7. Heroux MA, Bartlett RA, Howle VE, Hoekstra RJ, Hu JJ, Kolda TG, Lehoucq RB, Long KR, Pawlowski RP, Phipps ET, Salinger AG, Thornquist HK, Tuminaro RS, Willenbring JM, Williams A, Stanley KS. An overview of the Trilinos project. *ACM Transactions on Mathematical Software* 2005; **31**(3):397–423.
8. Bochev P, Ridzal D, Peterson K. *Intrepid: Interoperable Tools For Compatible Discretizations*. Sandia National Laboratories: Albuquerque, NM, 2010. (Available from: <http://trilinos.sandia.gov/packages/intrepid/>).
9. Gee MW, Siefert CM, Hu JJ, Tuminaro RS, Sala MG. ML 5.0 Smoothed Aggregation User’s Guide. *Technical Report SAND2006-2649*, Sandia National Laboratories, Albuquerque, NM, 2006.
10. Baker GA, Jureidini WN, Karakashian OA. Piecewise solenoidal vector fields and the Stokes problem. *SIAM Journal on Numerical Analysis* 1990; **27**(6):1466–1485.
11. Gunzburger MD. *Finite Element Methods for Viscous Incompressible Flows*. Academic Press: Boston, 1989.
12. Ciarlet P. *The Finite Element Method for Elliptic Problems*, SIAM Classics in Applied Mathematics. SIAM: Philadelphia, 2002.
13. Ern A, Guermond J-L. *Theory and Practice of Finite Elements*, no. 159 in Applied Mathematical Sciences. Springer Verlag: New York, 2004.
14. Cockburn B, Li F, Shu C-W. Locally divergence-free discontinuous Galerkin methods for the Maxwell equations. *Journal of Computational Physics* 2004; **194**(2):588–610.
15. Karakashian O, Katsaounis T. Numerical simulation of incompressible fluid flow using locally solenoidal elements. *Computers & Mathematics with Applications* 2006; **51**(9-10):1551–1570.
16. Crouzeix M, Raviart P. Conforming and nonconforming finite element methods for solving the stationary Stokes equations. *RAIRO-Mathematical Modelling and Numerical Analysis* 1973; **3**:33–76.
17. Bochev P, Gunzburger M. Analysis of least-squares finite element methods for the Stokes equations. *Mathematics of Computation* 1994; **63**:479–506.
18. Bolton P, Thatcher RW. On mass conservation in least-squares methods. *Journal of Computational Physics* 2005; **203**(1):287–304.

19. Chang CL, Nelson JJ. Least-squares finite element method for the Stokes problem with zero residual of mass conservation. *SIAM Journal on Numerical Analysis* 1997; **34**(2):480–489.
20. Heys JJ, Lee E, Manteuffel TA, McCormick SF. An alternative least-squares formulation of the Navier–Stokes equations with improved mass conservation. *Journal of Computational Physics* 2007; **226**(1):994–1006.
21. Heys JJ, Lee E, Manteuffel TA, McCormick SF, Ruge JW. Enhanced mass conservation in least-squares methods for Navier–Stokes equations. *SIAM Journal of Scientific Computing* 2009; **31**(3):2303–2321.
22. Jiang B-N, Chang C. Least-squares finite elements for the Stokes problem. *Computer Methods in Applied Mechanics and Engineering* 1990; **78**:297–311.
23. Jiang B-N, Sonnad V. Least-squares solution of incompressible Navier–Stokes equations with the p -version of finite elements. *Technical Report 91-14*, ICOMP, NASA, Cleveland, 1991.
24. Bochev P. Negative norm least-squares methods for the velocity–vorticity–pressure Navier–Stokes equations. *Numerical Methods for Partial Differential Equations* 1999; **15**:237–256.
25. Bramble JH, Pasciak JE. Least-squares methods for Stokes equations based on a discrete minus one inner product. *Journal of Computational and Applied Mathematics* 1996; **74**(1-2):155–173.
26. Raviart PA, Thomas JM. A mixed finite element method for second order elliptic problems. In *Mathematical Aspects of the Finite Element Method, I*, Galligani, Magenes E (eds), no. 606 in Lecture Notes in Math. Springer-Verlag: New York, 1977; 293–315.
27. Kanschhat G, Riviere B. A strongly conservative finite element method for the coupling of Stokes and Darcy flow. *Journal of Computational Physics* 2010; **229**(17):5933–5943.
28. Kanschhat G. Divergence-free discontinuous Galerkin schemes for the Stokes equations and the mac scheme. *International Journal for Numerical Methods in Fluids* 2008; **56**(7):941–950.
29. Bochev P. Analysis of least-squares finite element methods for the Navier–Stokes equations. *SIAM Journal on Numerical Analysis* 1997; **34**(5):1817–1844.
30. Bochev P, Choi J. A comparative study of least-squares, SUPG and Galerkin methods for convection problems. *International Journal of Fluid Dynamics* 2001; **15**(2):127–146.
31. Bazilevs Y, Hughes T. Weak imposition of Dirichlet boundary conditions in fluid mechanics. *Computers & Fluids* 2007; **36**:12–26. Challenges and Advances in Flow Simulation and Modeling.
32. Ghia U, Ghia KN, Shin CT. High-Re solutions for incompressible flow using the Navier–Stokes equations and a multigrid method. *Journal of Computational Physics* 1982; **48**(3):387–411.